# Climatology of aerosol optical properties and black carbon mass absorption cross section at a remote high altitude site in the Western Mediterranean Basin

Pandolfi, M.[1,*], Ripoll, A.[1], Querol, X.[1], and Alastuey, A[1].

[1] Institute of Environmental Assessment and Water Research (IDAEA-CSIC), Barcelona, Spain.

[*] corresponding author: marco.pandolfi@idaea.csic.es

## ABSTRACT

Aerosol light scattering ($\sigma_{sp}$), backscattering ($\sigma_{bsp}$) and absorption ($\sigma_{ap}$) were measured at Montsec (MSC; 42º3'N, 0º44'E , 1570 m a.s.l.), a remote high-altitude site in the Western Mediterranean Basin. Mean (±sd) $\sigma_{sp}$, $\sigma_{bsp}$ and $\sigma_{ap}$ were 18.9±20.8 $Mm^{-1}$, 2.6±2.8 $Mm^{-1}$ and 1.5±1.4 $Mm^{-1}$, respectively at 635 nm during the period under study (06/2011-06/2013). Mean values of single scattering albedo (SSA, 635 nm), scattering Ångström exponent (SAE, 450-635 nm), backscatter-to-scatter ratio (B/S, 635 nm), asymmetry parameter (g, 635 nm), black carbon mass absorption cross section (MAC, 637 nm) and $PM_{2.5}$ mass scattering cross section (MSCS, 635 nm) were 0.92±0.03, 1.56±0.88, 0.16±0.09, 0.53±0.16, 10.9±3.5 $m^2/g$ and 2.5±1.3 $m^2/g$ respectively. The scattering measurements performed at MSC were in the medium/upper range of values reported by Andrews et al. (2011) for other mountaintop sites in Europe due to the frequent regional recirculation scenarios (SREG) and Saharan dust episodes (NAF) occurring mostly in spring/summer and causing the presence of polluted layers at the MSC altitude. However, the development of up-slope winds and the possible presence of planetary boundary layer air at MSC altitude in summer may also have contributed to the high scattering observed. Under these summer conditions no clear diurnal cycles were observed for the measured extensive aerosol optical properties ($\sigma_{sp}$, $\sigma_{bsp}$ and $\sigma_{ap}$).

Conversely, low $\sigma_{sp}$ and $\sigma_{ap}$ at MSC were measured during Atlantic advections (AA) and winter regional anticyclonic episodes (WREG) typically observed during the cold season in the Western Mediterranean. Therefore, a season-dependent decrease in the magnitude of aerosol extensive properties was observed when MSC was in the free troposphere with the highest *free-troposphere vs all-data* difference observed in winter and the lowest in spring/summer. The location of MSC station allowed a reliable characterization of aerosols as a function the main synoptic meteorological patterns. The SAE was the lowest during NAF and showed an inverse correlation with the outbreaks intensity indicating a progressive shift toward larger particles. Moreover, the strength of NAF episodes in the region led to a slope of the scattering vs absorption relationship among the lowest reported for other mountain top sites worldwide indicating that MSC was dominated by dust aerosols at high aerosol loading. As a consequence, SSA showed a nearly monotonic increase with increasing particle concentration and scattering. The SAE was the highest during SREG indicating the presence of polluted layers dominated by smaller particles. Correspondingly, the asymmetry parameter was lower under SREG compared with NAF. The MAC and MSCS were significantly higher during NAF and SREG compared to AA and WREG indicating an increase of absorption and scattering efficiencies associated with the summer polluted scenarios. The optical measurements performed at the MSC remote site were compared with those simultaneously performed at a regional background station in the Western Mediterranean Basin located at around 700 m a.s.l. upstream the MSC station.

## 1. INTRODUCTION

Atmospheric aerosols affect the Earth's radiative balance directly, by scattering and absorbing solar and terrestrial radiation, and indirectly, by acting as cloud condensation nuclei, thus modifying the physical and optical properties of clouds. The measurements of aerosol optical properties such as scattering, backscattering, absorption, and extinction are important for aerosol characterization and model validation and, consequently, for a better comprehension of the role of aerosols in the Earth-atmosphere system (IPCC, 2007; IPCC, 2013). Specific aerosol optical parameters such as single scattering albedo (SSA), scattering Ångström exponent (SAE), backscatter-to-scatter ratio (B/S) and asymmetry parameter (g), among others, can be derived from these optical properties. Moreover, the mass scattering cross section (MSCS) and the mass absorption cross section (MAC) of sampled aerosols can be obtained from independent measurements of particulate matter (PM) and elemental carbon (EC) concentrations, respectively, and the measured aerosol scattering and absorption coefficients. The cooling or absorbing potential of atmospheric aerosols mostly depends on these parameters which are complex function of aerosols size, shape, chemical composition and refractive index. Most particles scatter the sun light causing a net cooling at the top of the atmosphere, whereas black carbon (BC) particles (or EC) absorb radiation over the entire visible spectrum thus affecting the vertical heating profile and causing a net warming of the Earth-atmosphere system (IPCC, 2007; IPCC, 2013). BC particles play a role second only to carbon dioxide in climate change and are co-emitted with a variety of other aerosols and precursor gases which can increase the light absorption by BC through an increase in its MAC (e.g. Bond et al., 2013). Given that atmospheric models convert the modelled BC mass concentrations to optical absorption using the MAC,

accurate estimates of MAC values and of the possible reasons explaining their variability are important.

Aerosol optical measurements are carried out worldwide by both in-situ and remote techniques. In order to address the uncertainties related with the geographical variation in aerosols optical properties, networks such as ACTRIS (Aerosols, Clouds, and Trace gases Research InfraStructure Network; www.actris.net) or the NOAA's baseline observatory (http://www.esrl.noaa.gov/gmd/) were created. The ACTRIS network aims at integrating three existing European research infrastructures: EUSAAR (European Supersites for Atmospheric Aerosol Research; for in-situ aerosol measurements at regional level; www.eusaar.net), EARLINET (European Aerosol Research Lidar Network, for remote aerosol measurements; www.earlinet.org) and CLOUDNET (to provide a systematic evaluation of clouds in forecast models, www.met.rdg.ac.uk/radar/cloudnet/). Thus, the ACTRIS project provides the unique opportunity to integrate in-situ and vertical aerosol measurements for the characterization of both the planetary boundary layer (PBL) and the free troposphere (FT). The measurements of aerosols in the FT are especially important given that FT aerosols are more spatially representative of the global atmosphere than the aerosols in the PBL due to their long residence time (of the order of several weeks). Aerosols in the FT can be transported over long distances and have extended climate and air quality impacts (Laj et al., 2009; Andrews et al., 2011). Due to the location of the majority of in-situ ACTRIS stations, the in-situ measurements are performed mainly within the PBL whereas the vertical lidar measurements allow for aerosol optical measurements almost in the whole troposphere. However, lidars do not measure key climate variables such as aerosol absorption, SSA, MSCS or MAC. Consequently, the measurements performed at mountaintop observatories provide the opportunity to make long-term,

100 continuous observations of in-situ aerosol properties in the free troposphere (FT).
101 Moreover, given their frequent position in the FT, mountaintop stations give the
102 possibility to study aerosols under different atmospheric scenarios without strong
103 interference from closer anthropogenic emissions. However, the number of mountaintop
104 observatories providing long-term in-situ aerosol optical measurements worldwide is
105 rather low. Recently, Andrews et al. (2011) presented climatology for free tropospheric
106 aerosol radiative properties utilizing in-situ data from ten high altitude stations in the
107 20–50ºN latitude band. Examples of high altitude aerosol optical measurements were
108 presented by Bodhaine (1983; 1995), McKendry et al. (2011), Marcq et al. (2010),
109 Collaud Coen et al. (2004, 2007, 2011), Cozic et al. (2008), Andrews et al. (2011),
110 Nyeki et al. (1998).

111 In this work we present the results from two year measurements (06/2011-
112 06/2013) of aerosol optical properties performed at the high altitude Montsec station
113 (MSC) which is run following the ACTRIS standards. Data from MSC were compared
114 with data collected at the ACTRIS Montseny station (MSY, 41º19'N, 02º21'E, 720 m
115 a.s.l.): a regional background station located around 140 km East from MSC. Seasonal
116 and diurnal variation of extensive (scattering, absorption, extinction) and intensive
117 (SSA, SAE, B/S, and $g$) aerosol properties and of MSCS and MAC are presented and
118 discussed. The effects of four main season-dependent synoptic atmospheric scenarios
119 affecting the Western Mediterranean Basin (WMB) on the measured optical properties
120 are also discussed. Moreover, the data collected when the MSC station is in the FT are
121 compared with the free tropospheric aerosol optical properties presented in Andrews et
122 al. (2011) for other mountaintop sites. All acronyms used in this work are reported in
123 Table 1.
124

## 2. Measurement site and methodology

### *2.1 Montsec measurement station*

The MSC site (42º3'N, 0º44'E , 1570 m a.s.l.) is a high altitude emplacement located in the NE of the Iberian Peninsula (Figure 1) and situated in the southern side of the Pre-Pyrenees at the top of the Montsec d'Ares mountain. This region is low-density populated and isolated from large pollutant emissions, 140 km from the highly urbanized and industrialized coastline to the SE, 30 km from the largest city around the region (Balaguer, 15,769 inhabitants) to the S, and 50 km from the axial Pyrenees to the N. The ACTRIS regional background station of MSY is located around 140 km from MSC site. Figure 1 also shows three meteorological stations: Montsec Observatory (800 m), Os de Balaguer (576 m) Vallfogona de Balaguer (238 m).

Aerosol measurements presented in this work were performed at MSC during the period 06/2011 – 06/2013. Due to the deployment of the nephelometer in measurement campaigns at other locations, scattering and backscattering data were not available from 02/2012 to 06/2012. Results from MSC site were compared with those simultaneously obtained at the MSY station (Figure 1). A description of the MSY site and of the optical measurement performed at MSY can be found in Pandolfi et al. (2011).

### *2.2 Optical Measurements*

#### *2.2.1 Scattering, hemispheric backscattering and absorption*

Particle scattering ($\sigma_{sp}$; 10–171º) and hemispheric backscattering ($\sigma_{bsp}$: 90–171º) coefficients at three wavelengths (450nm, 525nm, 635nm) were measured with a LED-based integrating nephelometer (model Aurora 3000, ECOTECH Pty, Ltd, Knoxfield, Australia). The $\sigma_{sp}$ and $\sigma_{bsp}$ data were corrected for truncation errors, allowing reporting scattering for 0-360º and backscattering for 90-270º, and for non-ideal (non-

150 Lambertian) illumination function of the light source as described by Müller et al.
151 (2011a). Müller et al. (2011a) provided parameterized correction factors for each
152 wavelength as linear relationship of the Ångström exponents calculated from
153 uncorrected multi-wavelength scattering measurements. A full calibration of the
154 nephelometer was performed four times per year by using $CO_2$ as span gas while zero
155 measurements and adjusts were performed once per week by using internally filtered
156 particle free air.

157 In order to reduce the effects of hygroscopicity enhancing the scattering
158 properties of particles, a relative humidity (RH) threshold of 40% was set in the
159 sampling cell by using a processor-controlled automatic heater inside the nephelometer.
160 This experimental procedure, which follows the ACTRIS standards, was applied
161 elsewhere (see for example Pereira et al., 2011; Anderson and Ogren, 1998; Pandolfi et
162 al., 2011). The mean RH in the nephelometer sampling cell during the study period was
163 28.4±9.5%. Moreover, in-cloud data were removed by selecting only those data with
164 ambient RH<90%. The detection limits of Aurora 3000 over one minute averaging time
165 are 0.11, 0.14, 0.12 $Mm^{-1}$ for total scattering at 450, 525, and 635 nm, respectively, and
166 0.12, 0.11, 0.13 $Mm^{-1}$ for backscattering (Müller et al., 2011a).
167 Aerosol absorption coefficients ($\sigma_{ap}$) at 637 nm (Müller et al., 2011b) were measured
168 with Multi Angle Absorption Photometers (MAAP, model 5012, Thermo). The
169 detection limit of the MAAP instrument is lower than 0.6 $Mm^{-1}$ over 2 min integration.
170 Absorption measurements are converted by the MAAP's software to BC concentration
171 (in $\mu g/m^3$) assuming a constant MAC of 6.6 $m^2/g$ (Petzold et al., 2004).

172 The nephelometer and MAAP instruments were connected to two separated
173 sampling lines with cut-off diameters of 2.5 μm and 10 μm, respectively, and placed at
174 about 1.5m above the roof of the cabin hosting the instruments. The inlets flow was $1m^3$

175 $h^{-1}$ and humidity control was performed by connecting a drier to the sampling inlet. The
176 Reynolds number for the described inlets was around 1300. The scattering,
177 backscattering and absorption measurements reported in this work were adjusted to
178 standard temperature and pressure (STP, $T_{standard}$=273.15 K and $P_{standard}$=1013.25).
179
180 *2.3 PM measurements*
181 Real time $PM_{10}$, $PM_{2.5}$ and $PM_1$ mass concentrations were continuously measured, on an
182 hourly base, by using a GRIMM optical counter (model 1107). Subsequently, the $PM_x$
183 concentrations were corrected with factors obtained by comparing the real time and
184 simultaneous in situ gravimetric measurements (Querol et al., 2008). $PM_x$ gravimetric
185 measurements on a 24h base were performed twice per week with high volume (Hi-Vol)
186 samplers (DIGITEL and MCV at 30$m^3$ $h^{-1}$) with appropriate $PM_x$ cut-off inlets.
187
188 *2.4 EC measurements*
189 The sampled 24h filters from Hi-Vol were analysed by means of a SUNSET OCEC
190 analyzer for the determination of elemental carbon (EC) concentrations. The EUSAAR
191 2 protocol (Cavalli et al., 2010) was used. In this work the uncertainties for the
192 measured EC concentrations were calculated by adding half of the minimum measured
193 EC concentration to the 7% of the concentrations (Err[EC] = min[EC]/2 + 0.07·[EC]).
194 With the EUSAAR 2 protocol the EC uncertainties have been estimated around 2-7 %
195 (JRC report, 2009). The formula applied here gives higher uncertainty to low EC
196 concentrations (e.g. Polissar et al., 1998).
197
198
199

200 *2.5 Data processing*

201 In this work the aerosol scattering, backscattering and absorption coefficients were
202 integrated over 1 h. Six additional parameters (B/S, *g*, SSA, SAE, MSCS and MAC)
203 were derived from the aerosol optical and mass concentration measurements. The B/S
204 parameter, which is the ratio between hemispherical backscatter and total scatter, is used
205 here to estimate the *g* of airborne particles used in radiative transfer calculations
206 (Andrews et al., 2006). Values of *g* can range from -1 for 180º backwards scattering to
207 +1 for complete forward scattering (0º), with a value of 0.7 commonly used in radiative
208 transfer models (Ogren et al., 2006). Following Delene and Ogren (2002) and Andrews
209 et al. (2006), *g* was calculated for the three nephelometer wavelengths as follows:

210

211 $$g = -7.14(B/S)^3 + 7.46(B/S)^2 - 3.96(B/S) + 0.9893 \quad (1)$$

212

213 The SSA indicates the relative amounts of radiation scattered and absorbed by
214 particles. Thus, SSA is a parameter indicating the potential for aerosols for cooling or
215 warming the atmosphere. It is defined as:

216

217 $$SSA = \frac{\sigma_{sp}}{\sigma_{sp} + \sigma_{ap}} \quad (2)$$

218 Non-absorbing particles such as sulfate have an SSA of one (cooling) while lower SSA
219 values indicate the presence of more absorbing particles. BC particles have an SSA of
220 about 0.2 (warming). In this work SSA was estimated at 635 nm, as the difference
221 between absorption at 637 nm (MAAP wavelength) and 635 nm was assumed to be
222 negligible.

223 The SAE (450-635 nm) was calculated from the multiwavelenghts nephelometer
224 data as:
225
226 $$SAE = -\frac{\log\left(\sigma_{sp}^{\lambda_1} / \sigma_{sp}^{\lambda_2}\right)}{\log\left(\lambda_1 / \lambda_2\right)} \quad (3)$$
227
228 The SAE describes the λ-dependence of particle scattering coefficient. An Ångström
229 exponent of 4 represents the scattering from molecules (Rayleigh's regime). A large
230 SAE (higher than 2) implies scattering dominated by submicron particles, while SAE
231 values lower than one represent an aerosol distribution dominated by coarser particles
232 (e.g. Schuster et al., 2006).
233 In order to eliminate issues with measurement noise during clean periods (e.g., when
234 MSC was in the FT), the B/S, g, SSA and SAE parameters were calculated from hourly-
235 averaged scattering (635 nm), hemispheric backscattering (635 nm) and absorption
236 above 0.4 $Mm^{-1}$, 0.4 $Mm^{-1}$ and 0.6 $Mm^{-1}$, respectively.
237 The MAC and MSCS are a measurement of the efficiency of the measured
238 particles to absorb or scatter, respectively, light at a given wavelength and are expressed
239 in $m^2/g$. The MAC is the parameter used to convert absorption to concentration of
240 absorbing particles (i.e. BC or EC) and *vice versa* and was estimated from error-
241 weighted linear fitting between $\sigma_{ap}$ from MAAP and EC concentrations from off-line
242 filter analysis. MAAP data were averaged over the filter sampling time. The MSCS is
243 the parameter relating the measured scattering with the concentration of PM and was
244 estimated at the three nephelometer wavelengths by averaging the ratios between $\sigma_{sp}$
245 and $PM_{2.5}$ after subtracting the EC mass from PM.

246 *2.6 Main meteorological patterns*

247 In order to determine and classify the atmospheric episodes affecting MSC, HYSPLIT
248 (http://ready.arl.noaa.gov/HYSPLITtraj.php), BSC/DREAM8b (http://www.bsc.es/proj
249 ects/earthscience/DREAM), SKIRON (http://forecast.uoa.gr/dustindx.php) and NAAPS
250 (http://www.nrlmry.navy.mil/aerosol) models were used. 120-hours backward
251 trajectories (for 12 p.m. modeling vertical velocity and for 3 different heights, 750, 1500
252 and 2500 m.a.g.l) were computed for each day of measurements, and classified
253 according to their predominant transport direction in: 1) Atlantic Ocean (AA; Atlantic
254 North and Atlantic North-West; 52%), 2) North Africa (NAF; 14%), 3) Winter Regional
255 (WREG, from November to April; 6%), and 4) Summer Regional (SREG, from May to
256 October; 9%). The global atmospheric circulation has some seasonal oscillations, thus
257 MSC is more westerly and northerly influenced in winter, while in summer the
258 prevailing winds come from the South (Ripoll et al., 2014). Consequently, AA episodes
259 are more frequent in winter, whereas continental NAF air masses are more frequent in
260 summer (Pandolfi et al., 2014, 2011; Querol et al., 2009; Pey et al., 2009; Pérez et al.
261 2008; Rodríguez et al., 2001). The advection of clean Atlantic air masses clears out the
262 previously accumulated pollution in the aged air masses, leading to lower pollutant
263 concentrations. In summer the meteorology of the area is mainly characterized by long
264 dry periods, sporadic but occasionally heavy rains, and a prevalence of NAF outbreaks
265 (Rodriguez et al., 2004). The WREG and SREG scenarios represent mainly air masses
266 from the Iberian Peninsula (IP) (Rodriguez et al., 2004). In winter (WREG) recurrent
267 anticyclonic conditions with weak synoptic winds lead to stagnation of air masses and
268 to the accumulation and aging of pollutants over the region. Under these conditions the
269 planetary boundary layer (PBL) height mostly determines the dilution of pollutants
270 around the emission sources and the degree of pollution at more elevated/regional areas

271 in the WMB (e.g. Jorba et al., 2013; Pandolfi et al., 2014). In summer, due to the intense
272 and rapid solar heating of the lower atmospheric layers, convergence of surface winds
273 from the coast to the central IP plateau injects polluted air into the middle troposphere
274 up to 3.5-5 km (Millán et al., 1997; Pérez et al., 2004). This pattern allows the
275 recirculation and accumulation of aerosol and has the potential to form stratified
276 reservoir layers of aged pollutants which subside over the coastal area and the sea (e.g.
277 Millán et al., 1992, Gangoiti et al., 2001; Pérez et al., 2004).
278
279 **3 RESULTS AND DISCUSSION**
280 *3.1 General features*
281 Table 2 reports the statistics for the measured parameters, including means, standard
282 deviations, percentiles (1, 10, 25, 50, 75, 99 percentiles), minima and maxima values
283 and skewness. All parameters showed skewness higher than 1 with the exception of
284 SAE, MSCS and MAC, for which almost normal distributions (skewness close to zero)
285 were observed, and SSA and *g* both showing a negative skewness. Similar SSA
286 skewness was presented from Pandolfi et al. (2011) at the MSY regional background
287 measurement site. Negative skewness for *g* is a consequence of the high positive
288 skewness observed for B/S.
289 Hourly $\sigma_{sp}$ and $\sigma_{bsp}$ at 635 nm at MSC ranged between 0.1 and 161.1 $Mm^{-1}$ (mean±sd:
290 18.9±20.8 $Mm^{-1}$) and between 0.0 and 17.1 $Mm^{-1}$ (2.6±2.8 $Mm^{-1}$), respectively. Mean
291 values of $\sigma_{sp}$ and $\sigma_{bsp}$ at 450 nm and 525 nm are reported in Table 2. The $\sigma_{ap}$ (at 637
292 nm) ranged between about 0.0 and 12.6 $Mm^{-1}$ with a mean value of 1.5±1.4 $Mm^{-1}$. The
293 hourly $PM_1$ levels at MSC ranged between about 0.1 $\mu gm^{-3}$ and 49.9 $\mu gm^{-3}$ with mean
294 value of 5.3±4.5 $\mu gm^{-3}$.

As shown later the lowest scattering, backscattering and absorption at MSC were measured under AA and WREG episodes typically observed during the cold season in the WMB. Conversely, high $\sigma_{sp}$, $\sigma_{bsp}$ and $\sigma_{ap}$ were measured during NAF and SREG episodes which predominate in spring/summer.

A comparison between measurements performed at MSC with those reported for other high altitude sites is reported in the following of this section and in the next sections. It should be taken into account that in some cases the comparison may be affected by the different size cut-off of the particles sampled at the different sites. At the Jungfraujoch high alpine site (3580 m a.s.l.; whole air sampled), Fierz-Schmidhauser et al. (2010) reported mean $\sigma_{sp}$ at 550 nm of about 12 $Mm^{-1}$, by excluding NAF episodes, and around 20 $Mm^{-1}$, considering only the NAF episodes. At Izaña (Canary Islands, ~2400 km a.s.l.; $PM_{10}$ size cut-off ) mean $\sigma_{sp}$ and $\sigma_{ap}$ at 550 nm of about 10 $Mm^{-1}$ and 0.8 $Mm^{-1}$, respectively, have been measured (Andrews et al., 2011). Monte Cimone (Italy, ~2200 m a.s.l.; whole air sampled) registered mean $\sigma_{sp}$ and $\sigma_{ap}$ of around 11 $Mm^{-1}$ and 3 $Mm^{-1}$, respectively, and both parameters increased highly during Saharan dust outbreaks and wildfire emissions over North Africa (Andrews et al., 2011; Cristofanelli et al., 2009). The mean scattering and absorption values measured at MSC were lower than the values reported by Pandolfi et al. (2011) for the MSY regional background station (720 m a.s.l.; $PM_{10}$ size cut-off). Mean $\sigma_{sp}$ (635 nm) and $\sigma_{ap}$ (637 nm) at MSY were around 26.6 $Mm^{-1}$ and 2.8 $Mm^{-1}$, respectively, due to the higher influence of anthropogenic emissions in the lower boundary layer (MSY) compared with higher altitudes (MSC).

The mean B/S (525 nm), SAE (450-635 nm), SSA (635 nm) and $g$ (525) measured at MSC were 0.135±0.066, 1.56±0.88, 0.92±0.03 and 0.59±0.13, respectively. At the alpine Jungfraujoch site, Fierz-Schmidhauser et al. (2010) reported mean B/S,

SAE and SSA for dry aerosols (RH<20%) within the ranges 0.128-0.122, 1.787-1.671 and 0.91-0.93, respectively. The higher B/S measured at MSC was likely due to the lower size range measured at MSC ($PM_{2.5}$) compared with Jungfraujoch (whole air) whereas the lower SAE at MSC, despite the different size cut-off, may be an indication of the prevalence of slightly coarser aerosols at MSC. This difference was likely due to the fact that more large particles had time to deposit out or be removed via wet scavenging since the altitude of Jungfraujoch is about twice the MSC altitude.

At the MSY regional background station the mean B/S (525 nm), SAE (450-635 nm), SSA (635 nm) and g (525 nm) were different by around -16%, +5%, -4% and +6%, respectively, compared to MSC (only contemporary data were used). These differences were small suggesting, on average, similarity in microphysical aerosol properties measured at MSC and MSY stations. Recently, Ripoll et al. (2014) have shown that the mean chemical composition of particles at MSC and MSY is on average similar mainly due to the frequency of specific meteorological episodes affecting aerosol properties similarly at both sites. The main difference was observed for B/S which was higher at MSC likely because the lower size cut-off at MSC ($PM_{2.5}$) compared to MSY ($PM_{10}$). Moreover, the relatively lower SSA and higher SAE at MSY, despite the differences in the size cut-off, suggested the presence of relatively smaller and more absorbing particles at regional level likely because the proximity of MSY station to anthropogenic sources.

The mean MAC (±sd) at MSC was around 11±4 $m^2/g$ and ranged from 2.4 to 20.8 $m^2/g$. Mean MSCS (±sd) at 635 nm, 525 nm and 450 nm were 2.5±1.4 $m^2/g$, 3.3±1.9 $m^2/g$ and 4.2±2.4 $m^2/g$, respectively. As shown later (section 3.5) the MAC and MSCS at MSC showed a clear seasonal dependence. These two parameters can change as a function of aerosol composition and age, and therefore it can differ depending on

345 the area under study and the meteorological scenarios. MAC between 7 $m^2/g$ and 20
346 $m^2/g$ have been often reported in literature (e.g. Quinn and Bates, 2005; Bond and
347 Bergstrom, 2006; Fernandez-Camacho et al., 2010; Arnott et al., 2003, 2005; Reche et
348 al., 2011; Pandolfi et al., 2011; Querol et al., 2013).
349
350 *3.2 Diurnal cycles and cluster analysis*
351 As shown in Fig.2 the mean scattering and absorption at MSC exhibited diurnal
352 cycles with lower values at night and higher values in the afternoon. Thus, on average,
353 thermally driven upslope winds and PBL height variations favoured the transport of
354 pollutants toward the MSC site during the warmest hours of the day. Similar diurnal
355 variations at other mountain top sites have been observed for extensive aerosol optical
356 properties (e.g. Andrews et al., 2011) and physical properties (e.g. Venzac et al., 2009;
357 Marinoni et al., 2008). The absolute values of extensive optical properties and PM mass
358 concentrations and their diurnal cycle amplitudes were higher at MSY site compared to
359 MSC (Fig.2) mainly because the proximity of MSY to the highly
360 urbanized/industrialized coastline (Fig.1) and its lower altitude compared to MSC. As a
361 consequence, the SSA and SAE at MSY station also showed marked diurnal cycles
362 compared to MSC due to the effectiveness of thermally-driven up-slope winds in
363 transporting fine highly absorbing particles of anthropogenic origin to MSY (Fig.2; cf.
364 Pandolfi et al., 2014).
365 The $\sigma_{sp}$ and $\sigma_{ap}$ measured at MSC showed marked differences as a function of
366 the different synoptic scenarios with the lowest values measured under AA and WREG
367 and the highest measured under NAF and SREG (Fig.2). The mean scattering at MSC
368 under NAF and SREG scenarios were close to the values measured at the MSY regional
369 background station, whereas lower scattering was measured at MSC under AA and

370 WREG compared to MSY. A similar pattern was observed for fine $PM_1$ concentrations
371 (Fig.2). The similarities in $\sigma_{sp}$ at MSC and MSY under NAF and SREG demonstrate the
372 potential of these two summer atmospheric scenarios in polluting both regional and
373 remote areas in the WMB. The potential of SREG scenarios to produce atmospheric
374 reservoir layers of aged pollutants is demonstrated also by the similarity in the
375 concentrations of fine PM at both sites despite their different altitude and distance from
376 important pollution sources. Conversely, mean $\sigma_{sp}$ and $PM_1$ concentrations at MSC
377 under WREG were relatively lower compared to MSY despite the general winter
378 anticyclonic conditions in the WMB which favour the accumulation of pollutants
379 around the emission sources. However, as already stated, the degree of pollution at
380 rural/remote elevated areas under WREG strongly depends on PBL height. We will
381 show later that MSC was predominantly in the free troposphere in winter when WREG
382 scenarios were observed. Conversely, during WREG the height of the polluted PBL can
383 often reach the MSY altitude (Pandolfi et al., 2014). The absorption measured at MSC
384 was lower compared with MSY for all considered scenarios due to the proximity of the
385 MSY station to anthropogenic sources of BC compared to MSC. As a consequence, the
386 SSA was higher at MSC than at MSY irrespective of the atmospheric scenarios. The
387 highest SSA at both sites was measured under NAF scenarios due to the higher relative
388 concentrations of dust particles from Africa enhancing the scattering. Finally, the SAE
389 showed similar characteristics at the two sites with lower values observed under NAF
390 (due to the transport of coarser particles) and higher values under SREG (due to the
391 increased relative concentration in the atmosphere of fine ($PM_1$) particles of
392 anthropogenic origin).
393
394

### *3.3 FT conditions at MSC station*

#### *3.3.1 Identification of FT air*

For the identification of *FT* air we followed the definition given by Andrews et al. (2011; AND2011 from now on) based on the use of data collected between 3 and 9 LT. As reported in AND2011, this criterion appears to be reasonable for most mountaintop sites and seasons. The limitations of this "time of day" approach are related to the location, height and topography of the site which determine the strength and frequency of local thermally-driven flow and the presence/intensity of polluted residual layers. All these factors make it difficult to rigorously define FT air. In the WMB the frequent SREG and NAF episodes in spring/summer further complicate the identification of the FT air. In order to evaluate when the MSC station was in the FT, we used meteorological data collected at MSC and at three lower altitude meteorological stations (Fig. 1). Thus, contemporary meteorological data collected at MSC station (1570 m a.s.l.), Montsec Observatory (800 m), Os de Balaguer (576 m) and Vallfogona de Balaguer (238 m) were used to study the mean diurnal cycles of potential temperature (Fig.3a), relative humidity (Fig.3b) and water vapour mixing ratio (Fig.3c) as a function of altitude. The potential temperature and water vapour mixing ratio were calculated with the humidity conversion formulas provided by Vaisala (Vaisala Oyj, 2013). Moreover, the diurnal cycles of the gradients of potential temperature (Fig.3e) and actual temperature (Fig.3f) were also reported to study the strength of the nocturnal and diurnal thermal inversions between the four sites (i.e. between mountain and valley). This analysis may be affected be differences due to different instruments, calibration procedures or local features associated to a specific location (the MSC station and Vallfogona de Balaguer were around 35km apart). Consequently, we also simulated the mean seasonal PBL diurnal cycles at MSC (Fig.3d) by means of HYSPLIT model

(http://www.ready.noaa.gov/READYamet.php). Grey and yellow rectangles in Fig.3 highlight hours when the MSC station was within the PBL and the hours of the time of the day approach (from 3:00 to 9:00 local time) for the identification of FT air proposed by Andrews et al. (2011), respectively. In this analysis we assumed that in a well mixed mixing layer the water vapour mixing ratio and potential temperature should be nearly constant with altitude within the PBL. In the free troposphere the water vapour content and potential temperature will decrease and increase, respectively, with altitude. Moreover, if the mixing layer has a uniform distribution of water vapour throughout, then the relative humidity has to increase with altitude. Fig.3 shows that when the relative humidity at MSC was higher compared to the other three stations, the potential temperature and water vapour content were fairly similar. We used these conditions to define the PBL air (grey rectangles). Conversely, at night/early morning (yellow rectangles) the relative humidity at MSC was the lowest and the differences in potential temperature and water vapour content among the four stations were the highest. Moreover, the gradients of potential temperature and actual temperature show that strong inversions were on average observed at night between Observatory and Os de Balaguer with MSC station above the inversion. Conversely, the gradients were lower and rather similar when MSC was within the PBL (grey rectangles). Fig. 3 also shows that our estimation of PBL conditions obtained using meteorological data agrees satisfactorily with the simulation performed with HYSPLIT.

Thus, the MSC station was on average above the inversion at night-early morning and within the PBL during the warmest hours of the day in summer, spring and autumn. Thus, the presence of polluted PBL residual layers at MSC altitude at night cannot be excluded. Conversely, in winter the MSC was on average in the FT during the whole day.

445 Figure 4 shows that the highest diurnal cycle amplitude of scattering at MSC was
446 observed in winter, whereas in spring and summer no clear diurnal cycles were
447 observed. The remarkable diurnal cycle of aerosol scattering in winter was due to the
448 position of MSC station in the free troposphere, whereas thermally-driven flows can
449 transport pollutants toward MSC around midday. The observed reduced diurnal cycle
450 for scattering at MSC during spring and summer was mainly due to the frequent
451 occurrence of NAF and SREG episodes and to the possible presence of polluted residual
452 layers at night at the MSC altitude. The NAF and SREG scenarios were also linked with
453 high concentrations of PM and BC during the whole day by Ripoll et al. (2014). Thus,
454 as already observed by Venzac et al. (2009) for the Puy de Dôme station, the seasonal
455 change of *FT* data at MSC was in part due to the seasonal variability in air mass origin
456 and transport routes.
457
458 *3.3.2 FT vs. all data: Comparison with mountaintop sites presented in AND2011*
459 Figure 5 shows the median values for all period (06/2011 – 06/2013) and by season at
460 MSC for the six aerosol optical parameters presented in AND2011. MSC data were
461 scaled to a wavelength of 550 nm (used in AND2011) by using 1.6 as SAE (median
462 values for MSC; this work) and 1.4 as absorption Angstrom exponent (AAE). The AAE
463 was calculated from 1 month absorption measurements performed at MSC with a 7
464 wavelengths Aethalometer (model AE33, Magee Scientific). For MSC the values were
465 calculated for the whole period considered here (ALL; 06/2011-06/2013), as well as for
466 fall (SON), winter (DJF), spring (MAM) and summer (JJA). Red and yellow colours in
467 Fig. 5 represent *all-data* (averaged over 24h) and *FT-data* (averaged between 03:00
468 a.m. and 09:00 a.m. LT), respectively. The percentage values in each figure represent
469 the relative difference between the medians calculated for *all-data* and *FT-data*, with

positive values indicating lower *FT-data* medians compared to *all-data*. The non-parametric Mann–Whitney U test was applied to study whether the differences between *all-data* and *FT-data* medians were statistically significant. In Fig. 5 bold green numbers indicate statistically significant differences to a significance level of 5% (p-value < 0.05), blue bold numbers highlight marginally significant differences ($p < 0.1$) whereas black numbers report differences which were not statistically significant ($p > 0.1$). The six red and yellow rectangles within the blue areas on the right of each figure represent the range of variability of the medians presented by AND2011 calculated for mountaintop sites in the western hemisphere (W), Europe (EU) and eastern hemisphere (E).

As reported in Fig.5 the scattering (median 14.1 $Mm^{-1}$; Fig.5a ALL, *all-data*) and the absorption (1.2 $Mm^{-1}$; Fig.5b ALL, *all-data*) measured at MSC for the whole dataset (ALL) locate the MSC site in the medium/upper range of EU ranges. This is especially marked for scattering data. As reported in Fig.5 higher scattering and absorption at MSC were measured in summer (JJA, *all-data*; 34.6 $Mm^{-1}$ and 2.4 $Mm^{-1}$, respectively) compared to winter (DJF, *all-data*; 3.7 $Mm^{-1}$ and 0.3 $Mm^{-1}$, respectively). As already noted, the NAF and SREG episodes affecting the WMB have the potential to increase the aerosol mass and scattering measured in this area in summer (Fig.2 and JJA scattering in Fig.4). At the same time, the lower altitude of MSC station compared with the stations reported in AND2011 (lowest altitude around 2.2 km) may have also contributed to the relatively higher scattering observed at MSC station. Recently, Ripoll et al. (2014) have shown that the MSC site registers higher $PM_{10}$ concentrations than those measured at other high-altitude central European sites and similar or lower BC concentrations. As a consequence, the median value of SSA at MSC (0.93; Fig.5d ALL, *all-data*) was relatively higher compared with the EU, W and E ranges of

variability. Conversely, SAE (1.65; Fig.5e ALL, *all-data*) and B/S (0.126; Fig.5f ALL, *all-data*) were in the middle of the corresponding EU ranges. The SSA at MSC did not change considerably as a function of seasons and varied between 0.92 (SON) and 0.94 (DJF). Conversely, SAE was higher in summer (1.74; Fig.5e JJA, *all-data*) compared to winter (1.39; Fig.5e DJF, *all-data*). The relatively higher SAE observed in summer suggested the prevalence, on average, of finer particles at MSC compared to winter likely due to the frequent SREG scenarios observed during the warm season (cf. Fig.2). Accordingly, the lowest B/S was measured in winter (0.119; Fig.5f DJF *all-data*) and the highest in summer (0.130; Fig.5f JJA *all-data*).

All the extensive aerosol properties (scattering, absorption and extinction) showed relatively lower *FT-data* medians compared with *all-data* (16-19%; ALL in Figs. 5a,b,c). This was a common characteristic for most of the stations presented in AND2011. However, the relative decreases in *FT-data* extensive properties were clearly seasonal at the MSC site with the highest *FT* vs. *all-data* difference observed in winter (DJF in Figs.5a,b,c; 21-23%) and the lowest in spring/summer (MAM and JJA in Figs.5a,b,c; 0-8%). The differences between the *FT-data* and *all-data* medians were statistically significant for ALL, SON and DJF and marginally significant for JJA. As a consequence of the time of day segregation used for the identification of FT air (3:00–09:00 am vs. 24h) the remote sites showing stronger diurnal cycles tend to have larger decreases in *FT* aerosol loading compared to *all-data* (24h) aerosol loading (Andrews et al., 2011). In our case, the high *FT* vs. *all-data* difference observed in winter is consistent with the strong DJF diurnal cycle of normalized scattering presented in Fig.4. The lower *FT* vs. *all-data* difference in spring/summer was due to the occurrence of NAF and SREG episodes and to the fact that FT conditions were less frequent in spring/summer due to higher boundary layer. Finally, the differences between the *FT-*

520 *data* and *all-data* medians calculated for the intensive aerosol properties were
521 statistically significant only for SAE in winter (DJF) with slightly higher SAE observed
522 for FT air (1.47; Fig.5e DJF, *FT-data*).
523
524 *3.4 Relationships between $\sigma_{sp}$ and other extensive/intensive aerosol properties*
525 Figure 6 shows the relationships between $\sigma_{sp}$ and some of the measured extensive
526 (backscattering, absorption, $PM_1$ concentrations) and intensive (g, SAE, SSA) aerosol
527 properties. Relationships are presented for the whole database (ALL; highlighted by the
528 blue rectangle) and as a function of the main considered meteorological patterns (AA,
529 NAF, SREG, WREG). Similar relationships were investigated e.g. by Delene and Ogren
530 (2002), Pandolfi et al. (2011) and Andrews et al. (2011). However, to our knowledge
531 this is the first time that these relationships are presented as a function of air mass type.
532 These kind of relationships helps to constrain model parameterizations and to reduce
533 uncertainties in the algorithms used for deriving intensive aerosol properties from
534 remotely sensed data (Delene and Ogren, 2002). In Fig. 6 the frequency distribution of
535 scattering coefficient at 635 nm was calculated for values between 0 $Mm^{-1}$ and 90
536 $Mm^{-1}$ with a bin of 5 $Mm^{-1}$ for ALL and NAF scenario. For AA, SREG and WREG
537 scenarios the occurrence for high $\sigma_{sp}$ was lower thus limiting the frequency distributions
538 to 75 $Mm^{-1}$, 75 $Mm^{-1}$, and 55 $Mm^{-1}$, respectively.
539 As shown in Fig. 6 the frequency distribution of aerosol scattering was more right-
540 skewed during AA (sk = 1.93) and WREG (sk = 1.45) compared with NAF (sk = 0.92)
541 and SREG (sk = 0.83) when pollution levels at MSC were higher (Fig. 2).
542 As reported in Fig. 6 the backscattering and $PM_1$ concentrations increased with
543 increasing $\sigma_{sp}$. If the $PM_1$ concentrations increase the intensity of light scattered, and
544 also backscattered, increases almost monotonically. Also the absorption, which is

545 roughly proportional to the concentration of absorbing aerosols in PM samples,
546 increased with increasing scattering and $PM_1$ concentration. Similar findings were
547 reported by Pandolfi et al. (2011) for the MSY site and by AND2011 (Fig.6a in
548 AND2011) for the 10 stations considered in their paper. AND2011 observed that the
549 measurement sites which were dominated by dust aerosol at high aerosol loading tend to
550 have a lower slope of the scattering-absorption relationship than the other sites. This is
551 also the case at MSC which shows a scattering-absorption slope in the lower range of
552 those reported by AND2011 (cf. with Fig.6a in AND2011). Fig. 6 shows that the
553 increase of the extensive aerosol properties with increasing aerosol scattering was fairly
554 similar during the different considered meteorological scenarios thus leading to very
555 similar SSA as also reported in Fig. 2. Conversely, the most remarkable difference
556 among the scenarios was observed for SAE which decreased with increasing scattering
557 during NAF reaching values around 0.8 at $\sigma_{sp}$ =90 $Mm^{-1}$. Thus, the SAE was clearly a
558 function of NAF intensity. Conversely, during SREG SAE was higher and nearly
559 constant (around 1.8 for $0<\sigma_{sp}<90$ $Mm^{-1}$) indicating the prevalence of smaller particles
560 with a relatively lower g (0.53 during SREG compared with 0.57 during NAF). No
561 remarkable differences were observed for the intensive aerosol properties between the
562 less polluted WREG and AA scenarios.
563 On average (ALL in Fig. 6) the parameters g and SAE measured at MSC showed
564 inverse relationships with $\sigma_{sp}$: when $\sigma_{sp}$ increased above around 45-50 $Mm^{-1}$ SAE
565 decreased indicating the shift toward larger particles with relatively higher g and SSA.
566 The observed decrease of SAE was due to the prevalence of dust (i.e. large, primarily
567 scattering) particles at high aerosol load at MSC.
568 To further investigate the effect of NAF episodes on SAE we report in Figure 7 the
569 distribution of $\sigma_{sp}$ as a function of SAE by atmospheric scenarios (Fig.7a) and by levels

570 of $PM_1/PM_{10}$ ratio (Fig.7b). As shown in Fig.7a, high scattering and relatively low SAE
571 (<1) were associated with NAF episodes (yellow colour). Correspondingly, the
572 $PM_1/PM_{10}$ ratio was among the lowest (0.2-0.3; Fig.7b) indicating the prevalence of
573 coarser particles. The AA scenarios (blue colour in Fig. 7a) were mainly associated with
574 relatively lower scattering (11.7±13.9 $Mm^{-1}$ at 635 nm), a broad range of SAE values
575 (from -2 to 4) and $PM_1/PM_{10}$ ratios around 0.3-0.5. Cermac et al. (2010) suggested that
576 negative SAE could be an indication of reduced anthropogenic emissions with
577 prevalence of coarse-mode particles. For example negative SAE and high aerosol
578 optical depth (AOD) have been related with transport of coarse-mode dust in northern
579 India by Singh et al. (2004). However, extremely negative values of SAE are unfeasible
580 for atmospheric aerosols. Similarly, the SAE cannot be higher than about 4 which
581 represent the limit given by the Rayleigh regimen for the molecular scattering. In the
582 present case 123 hourly values of SAE out of 9561 were smaller than -1 (1.2%) and 150
583 values were higher than 4 (1.6 %). Consequently, the measured negative SAE at MSC
584 were likely due to both the presence of relatively larger particles during low aerosol
585 concentration (Fig. 7b) and the instrumental noise under low scattering conditions.
586 Similar behaviour of SAE was also observed in a remote subartic site by Aaltonen et al.
587 (2006) and at the MSY station by Pandolfi et al. (2011). Finally, the SREG episodes
588 mainly (red colours; Fig. 7a), and to a lesser extent WREG (orange colour), were
589 associated with relatively larger SAE compared with NAF and high $PM_1/PM_{10}$ ratios
590 indicative of the prevalence of mainly fine particles of anthropogenic origin.
591 For $\sigma_{sp}$ between around 20-40 $Mm^{-1}$ (ALL in Fig.6) both g and SAE showed relatively
592 constant values around 0.55 (g) and 1.65 (SAE) which were close to the averages
593 reported in Table 2 for these two parameters. When $\sigma_{sp}$ was below around 15-20 $Mm^{-1}$
594 SAE decreased indicating again the shift toward relatively larger particles associated

595 with relatively clean atmosphere ($PM_1$<5 $\mu gm^{-3}$). This decrease was more pronounced
596 for AA and WREG compared with NAF and SREG (Fig. 6). However, under very low
597 $PM_1$ concentrations at MSC ($PM_1$<1.5 $\mu gm^{-3}$) SSA and g reached very low values
598 around 0.84 and 0.43 (ALL in Fig. 6), respectively, whereas the SAE increased. These
599 low PM conditions at MSC were associated with the prevalence of small particles with
600 relatively higher absorption properties irrespective of the scenario considered. Low
601 values of SSA at very low aerosol loading have been observed in AND2011 and
602 associated with an aerosol mixture in which large scattering aerosol particles have been
603 preferentially removed (e.g., by cloud scavenging and/or deposition), leaving behind a
604 relatively smaller and darker aerosol (e.g., AND2011; Berkowitz et al., 2011; Marcq et
605 al., 2010; Targino et al., 2005; Sellegri et al., 2003).
606
607 3.5 MAC and MSCS climatology
608 Mean MAC, at Montsec determined as the error-weighted slope of the absorption-EC
609 scatterplot, was 11.1±0.3 $m^2/g$ ($R^2$=0.82). Given that $\sigma_{ap}$ and EC concentrations
610 measurements were available since the end of 2009, the mean MAC presented here was
611 calculated over the period November 2009 – June 2013 (384 sample pairs on 24h base).
612 Mean MSCS at 635 nm (228 sample pairs) was 2.5±1.3 $m^2/g$. MSCS at 525 nm and 450
613 nm are reported in Table 2. On average, lower MAC values were observed during AA
614 (9.7±0.7 $m^2/g$; $R^2$=0.77) and WREG (9.4±1.0 $m^2/g$; $R^2$=0.88) scenarios compared to
615 NAF (11.9±0.7 $m^2/g$; $R^2$=0.61) and SREG (12.6±1.0 $m^2/g$; $R^2$=0.74) scenarios.
616 Similarly, low MSCS was on average observed during AA and WREG (2.0±1.1 $m^2/g$
617 and 1.5±0.6 $m^2/g$, respectively at 635 nm) whereas MSCS was higher during NAF and
618 SREG (3.7±1.4 $m^2/g$ and 3.5±0.7 $m^2/g$, respectively). The non-parametric Kruskal-
619 Wallis test was used for testing the equality of medians among the four selected

620 categories (scenarios). The difference between the NAF and SREG medians was not
621 statistically significant ($p>0.5$) for both MAC and MSCS. The same was observed for
622 the AA and WREG medians ($p>0.3$). Conversely, statistically significant differences
623 ($p<0.001$) were observed between the medians calculated for WREG and AA and those
624 calculated for NAF and SREG. The higher MAC and MSCS under NAF and SREG
625 compared to AA and WREG were likely due to differences in particles origin and
626 particle properties during these scenarios. The SREG scenario is a summer scenario (cf.
627 Fig. 8) which favours the recirculation and aging of pollutants in the WMB. Several
628 publications have shown higher sulphate (e.g. Pey et al., 2009; Querol et al., 1999) and
629 organic matter concentrations (e.g. Querol et al., 2013; Pandolfi et al., 2014) in summer
630 compared to winter in the WMB at regional and remote levels. The summer sulphate
631 and organic matter maxima were due to higher temperatures and increased
632 photochemistry in the atmosphere enhancing the $SO_2$ oxidation and the formation of
633 secondary organic aerosols from biogenic emissions from vegetation (Seco et al., 2011).
634 Moreover, Ripoll et al. (2014) have shown higher concentrations of BC particles in the
635 warmer months at MSC attributed to the impact of the SREG episodes and to the higher
636 occurrence of wildfires in North Africa and/or in the WMB (Cristofanelli et al., 2009).
637 Once formed these particles can recirculate and age under SREG scenario in the WMB.
638 On the other hand the NAF scenarios, which are more frequent in summer in the WMB
639 (Pey et al., 2013), increase the concentration of mineral dust in the atmosphere.
640 Moreover, Rodríguez et al. (2011) and Ripoll et al. (2014) have shown that pollutants
641 such as sulphate and BC may be transported together with dust across the WMB during
642 NAF episodes.
643 The mixing of BC particles with other chemical components, such as sulphate and
644 organics, have the potential to increase the absorption properties of BC particles (e.g.

Bond et al., 2013) and could explain the higher MAC observed at MSC during NAF and SREG. At the same time also the MSCS was higher during NAF and SREG indicating higher scattering efficiency of PM. Similar dependence of the MAC with atmospheric scenarios was reported by Pandolfi et al. (2011) for Montseny station. Exception was observed for the MAC calculated at Montseny during WREG which was the highest compared to AA, SREG and NAF. The likely reason for the different MAC at MSC and MSY under WREG was the lower altitude of MSY station which was often within the polluted PBL under WREG winter scenarios (i.e. Pandolfi et al., 2014) whereas the MSC was above.

As a consequence of the observed variations of MAC and MSCS as a function of the four considered season-dependent scenarios, the MAC and MSCS at MSC showed a clear annual cycle with the lowest values observed in winter and the highest in summer (Figure 8). Similar seasonal dependence of the MAC with higher values in summer was observed at the Jungfraujoch high alpine site (Cozic et al., 2008).

## Conclusions

The measurements of aerosol optical properties presented in this work and performed at Montsec remote site (MSC; 42º3'N, 0º44'E, 1570 m a.s.l.) add useful information on the limited amount of in-situ aerosol optical data obtained at high altitude/mountaintop sites worldwide. The aerosol scattering measurements performed at MSC located this site in the medium/upper range of values reported for other mountaintop sites in Europe (EU). The frequent African dust (NAF) outbreaks and regional recirculation (SREG) scenarios, typical of the WMB in spring/summer, were mainly responsible for these relatively high values. Moreover, the lower altitude of MSC station compared with other mountaintop sites and the strong summer insolation in the Mediterranean regions,

favoring the development of thermally-driven up-slope winds, may have also contributed to the relatively higher scattering observed at MSC. The mean scattering at MSC during the NAF and SREG scenarios were close to the values measured at a regional background station (Montseny; 720 m a.s.l.) thus demonstrating the potential of these two summer atmospheric scenarios in polluting the whole lower troposphere in the Western Mediterranean. As a consequence, in spring and summer no clear diurnal cycles were observed for the extensive aerosol optical properties due to the presence of polluted layer at the MSC altitude. Thus, the diurnal variation of scattering at MSC during spring and summer was subject to synoptic circulation which masked in part the mountain breezes and the dynamics transport at a more local scale. Conversely, during Atlantic advection (AA) and winter regional anticyclonic (WREG) episodes, mainly registered during the cold season, the extensive aerosol properties at MSC were considerably lower compared to Montseny and the highest diurnal cycle amplitudes were observed. The AA scenario in the WMB is typically characterized by high wind speed with air masses coming from the Atlantic Ocean thus favouring the dispersion of the accumulated pollution with consequent reduction of the concentrations of pollutants which is more effective at remote level. The WREG scenario is mainly characterized by weak synoptic winds leading to stagnation of air masses and to the accumulation and aging of pollutants over the region, whereas the PBL height mostly determines the dilution of pollutants around the emission sources and the degree of pollution at more elevated/regional areas in the WMB. Absorption at MSC was not as high as scattering compared with most of measurements in EU thus leading to relatively higher single scattering albedo (SSA) compared with EU data. Conversely, the scattering Angstrom exponent (SAE) and backscatter-to-scatter ratios (B/S) were in the middle of the corresponding EU ranges.

All the extensive aerosol properties measured at MSC showed relatively lower medians when MSC was in the free troposphere (*FT-data*) compared with the whole database (*all-data*). These decreases were clearly seasonal at MSC site with the highest and statistically significant *FT* vs. *all-data* difference observed in winter and the lowest (and not statistically significant) in spring/summer. The frequent NAF and SREG scenarios in summer, and the less frequent FT conditions due to higher boundary layer, explained the lower *FT* vs. *all-data* differences observed in summer compared to winter.

The aerosol optical measurements performed demonstrated that the MSC measurement site provides reliable information for a suitable characterization of the main synoptic meteorological patterns affecting the region. Clear differences were observed between NAF and SREG scenarios in terms of intensive aerosol optical properties. SAE during NAF was the lowest, indicating presence of larger particles, and was clearly anticorrelated with the intensity of Saharan dust outbreaks, whereas nearly constant and higher SAE was measured under SREG indicating an aerosol mode dominated by finer particles. Correspondingly, the asymmetry parameter was higher during NAF compared to SREG. The analysis of the relationships between scattering and other extensive/intensive aerosol properties measured at MSC showed a scattering-absorption slope in the lower range of slopes calculated worldwide indicating that the MSC site is dominated by dust aerosols at high aerosol loading. As a consequence, SSA increased nearly monotonically with increasing scattering.

The MAC estimated at MSC showed a clear annual cycle with higher values in summer when the occurrence of NAF and SREG scenarios favoured the presence of polluted atmospheric layers containing aged BC particles likely mixed with other chemical components such as organics and sulfate. These summer conditions were also linked with higher scattering efficiency of PM.

**Acknowledgments**

This work was supported by the MINECO (Spanish Ministry of Economy and Competitiveness), the MAGRAMA (Spanish Ministry of Agriculture, Food Environment) and FEDER funds; the projects PRISMA (CGL2012-39623-C02/00) and VAMOS (CLG2010-19464). The research received funding from the European Union Seventh Framework Programme (FP7/2007-2013) ACTRIS under grant agreement no. 262254. M. Pandolfi was funded by the JAE-Doc CSIC program, co-funded by the European Social Fund (ESF). The authors wish to thank D. C. Carslaw and K. Ropkins for providing the Openair software used in this paper (Carslaw and Ropkins, 2012; Carslaw, 2012). The authors gratefully acknowledge HYSPLIT model, SKIRON, BSC-DREAM and NRL-NAAPS aerosol maps, NCEP/NCAR meteorological database NOAA NAO index data, and image products from MODIS and SeaWiFs NASA satellites used in this publication. The authors would like to extend their gratitude to the personnel from the OAdM. We would also like to express our gratitude to METEOCAT for the meteorological data.

**Bibliography**

Aaltonen, V., Lihavainen, H., Kerminen, V.-M., Komppula, M., Hatakka, J., Eneroth, K., Kulmala, M., and Viisanen, Y.: Measurements of optical properties of atmospheric aerosols in Northern Finland, Atmos. Chem. Phys., 6, 1155–1164, doi:10.5194/acp-6-1155-2006, 2006.

Anderson, T.L. and Ogren, J.A.: Determining Aerosol Radiative Properties Using the TSI 3563 Integrating Nephelometer, Aerosol Sci. Tech., 29, 57–69, 1998.

745

746 Andrews, E., Sheridan, P.J., Fiebig, M., McComiskey, A., Ogren, J.A., Arnott, P.,
747 Covert, D., Elleman, R., Gasparini, R., Collins, D., Jonsson, H., Schmid, B., and Wang,
748 J.: Comparison of methods for deriving aerosol asymmetry parameter, J. Geophys. Res.
749 Atmos., 111, D05S04, doi:10.1029/2004JD005734, 2006.

750

751 Andrews, E., Ogren, J. A., Bonasoni, P., Marinoni, A., Cuevas, E., Rodríguez, S., Sun,
752 J.Y., Jaffe, D.A., Fischer, E.V., Baltensperger, U., Weingartner, E., Collaud Coen, M.,
753 Sharma, S., Macdonald, A.M., Leaitch, W.R., Lin, N.-H., Laj, P., Arsov, T., Kalapov, I.,
754 Jefferson, A. and Sheridan, P.: Climatology of aerosol radiative properties in the free
755 troposphere, Atmos. Res., 102, 365–393, doi:10.1016/j.atmosres.2011.08.017, 2011.

756

757 Arnott, W.P., Moosmüller, H., Sheridan, P.J., Ogren, J.A., Raspet, R., Slaton, W.V.,
758 Hand, J.L., Kreidenweis, S.M., and Collett Jr., J.L.: Photoacoustic and Filter-Based
759 Ambient Aerosol Light Absorption Measurements: Instrument Comparisons and the
760 Role of Relative Humidity, J. Geophys. Res., 108(D1), 4034,
761 doi:10.1029/2002JD002165, 2003.

762

763 Arnott, W.P., Hamasha, K., Moosmüller, H., Sheridan, P. J., and Ogren, J.A.: Towards
764 Aerosol Light Absorption Measurements with a 7-wavelength Aethalometer: Evaluation
765 with a Photoacoustic Instrument and 3 wavelength Nephelometer, Aerosol Sci. Tech.,
766 39, 17–29, 2005

767

768 Berkowitz, C., Berg, L.K., Yu, X.-Y., Alexander, M.L., Laskin, A., Xie, Y., Jobson,
769 B.T., Andrews, E., Ogren, J.: A statistical overview of aerosol optical, chemical and

770 physical measurements at a coastal northern California site during the summer of 2005,
771 Atmos. Env., 45, 2559–2568, DOI 10.1016/j.atmosres.2011.08.017, 2011.
772
773 Bodhaine, B.: Aerosol measurements at four background sites, J. Geophys. Res. 88,
774 10,753–10, 768, DOI: 10.1029/JC088iC15p10753, 1983.
775
776 Bodhaine, B.: Aerosol absorption measurements at Barrow, Mauna Loa and the South
777 Pole. J. Geophys. Res. 100, 8967–8975, DOI: 10.1029/95JD00513, 1995.
778
779 Bond, T.C. and Bergstrom, R.W.: Light absorption by carbonaceous particles: An
780 investigative review, Aerosol Sci. Technol., 40, 27-67,
781 doi:10.1080/02786820500421,521, 2006.
782
783 Bond, T.C., Doherty, S.J., Fahey, D.W., Forster, P.M., Berntsen, T., DeAngelo, B.J.,
784 Flanner, M.G., Ghan, S., Kärcher, B., Koch, D., Kinne, S., Kondo, Y., Quinn, P.K.,
785 Sarofim, M.C., Schultz, M. G., Schulz, M., Venkataraman, C., Zhang, H., Zhang, S.,
786 Bellouin, N., Guttikunda, S.K., Hopke, P. K., Jacobson, M.Z., Kaiser, J.W., Klimont,
787 Z., Lohmann, U., Schwarz, J.P., Shindell, D., Storelvmo, T., Warren S.G., and Zender,
788 C.S.: Bounding the role of black carbon in the climate system: A scientific assessment,
789 J. Geophys. Res. 118, 11, 5380–5552, DOI: 10.1002/jgrd.50171, 2013.
790
791 Carslaw, D.C.: The openair manual – open-source tools for analysing air pollution data,
792 Manual for version 0.7-0, King's College, London, 2012.
793

794 Carslaw, D.C. and Ropkins, K.: openair – an R package for air quality data analysis,
795 Environ. Modell. Softw., 27–28, 52–61, 2012.
796
797 Cavalli, F., Viana, M., Yttri, K. E., Genberg, J., and Putaud, J.-P.: Toward a
798 standardised thermal-optical protocol for measuring atmospheric organic and elemental
799 carbon: the EUSAAR protocol, Atmos. Meas. Tech., 3, 79–89, doi:10.5194/amt-3-79-
800 2010, 2010.
801
802 Cermak, J., Wild, M., Knutti, R., Mishchenko, M.I., and Heidinger A.K.: Consistency
803 of global satellite-derived aerosol and cloud data sets with recent brightening
804 observations, Geophys. Res. Lett., 37, L21704, doi:10.1029/2010gl044632, 2010.
805
806 Collaud Coen, M.,Weingartner, E., Schaub, D., Hueglin, C., Corrigan, C., Henning, S.,
807 Schwikowski, M., Baltensperger, U.: Saharan dust events at the Jungfraujoch: detection
808 by wavelength dependence of the single scattering albedo and first climatology analysis,
809 Atmos. Chem. Phys., 4, 2465–2480, doi:10.5194/acp-4-2465-2004, 2004.
810
811 Collaud Coen, M., Weingartner, E., Nyeki, S., Cozic, J., Henning, S., Verheggen, B.,
812 Gehrig, R., Baltensperger, U.: Long-term trend analysis of aerosol variables at the high-
813 alpine site Jungfraujoch, J. Geophys. Res., 112, D13213. doi:10.1029/2006JD007995,
814 2007.
815
816 Collaud Coen, M.,Weingartner, E., Furger, M., Nyeki, S., Prévôt, A.S.H., Steinbacher,
817 M., Baltensperger, U.: Aerosol climatology and planetary boundary influence at the

818 Jungfraujoch analyzed by synoptic weather types, Atmos. Chem. Phys., 11, 5931–5944,
819 doi:10.5194/acp-11-5931-2011, 2011.
820
821 Cozic, J., Verheggen, B., Weingartner, E., Crosier, J., Bower, K.N., Flynn, M., Coe, H.,
822 Henning, S., Steinbacher, M., Henne, S., Collaud Coen, M., Petzold, A., and
823 Baltensperger, U.: Chemical composition of free tropospheric aerosol for PM1 and
824 coarse mode at the high alpine site Jungfraujoch, Atmos. Chem. Phys., 8, 407-423,
825 doi:10.5194/acp-8-407-2008, 2008.
826
827 Cristofanelli, P., Marinoni, A., Arduini, J., Bonafè, U., Calzolari, F., Colombo, T.,
828 Decesari, S., Duchi, R., Facchini, M. C., Fierli, F., Finessi, E., Maione, M., Chiari, M.,
829 Calzolai, G., Messina, P., Orlandi, E., Roccato, F., and Bonasoni, P.: Significant
830 variations of trace gas composition and aerosol properties at Mt. Cimone during air
831 mass transport from North Africa – contributions from wildfire emissions and mineral
832 dust, Atmos. Chem. Phys., 9, 4603-4619, doi:10.5194/acp-9-4603-2009, 2009.
833
834 Delene, D.J., Ogren, J.A.: Variability of aerosol optical properties at four North
835 American surface monitoring sites. J. Atmos. Sci. 59, 1135–1150, 2002.
836
837 Fernandez-Camacho, R., Rodríguez, S., de la Rosa, J., Sanchez de la Campa, A., Viana,
838 M.M., Alastuey, A., and Querol, X.: Ultrafine particle formation in the inland sea breeze
839 airflow in Southwest Europe, Atmos. Chem. Phys., 10, 9615–9630, doi:10.5194/acp-10-
840 9615-2010, 2010.
841

842 Fierz-Schmidhauser, R., Zieger, P., Gysel, M., Kammermann, L., DeCarlo, P. F.,
843 Baltensperger, U., and Weingartner, E.: Measured and predicted aerosol light scattering
844 enhancement factors at the high alpine site Jungfraujoch, Atmos. Chem. Phys., 10,
845 2319–2333, doi:10.5194/acp-10-2319-2010, 2010.
846
847 Gangoiti, G., Millán, M. M., Salvador, R., and Mantilla E.: Long-Range transport and
848 recirculation of pollutants in the western Mediterranean during the project Regional
849 Cycles of Air Pollution in the west-central Mediterranean Area, Atmos. Environ., 35,
850 6267–6276, 2001.
851
852 IPCC 2007 in: Climate Change 2007: The Physical Science Basis (Contribution of
853 Working Group I to the Fourth Assessment Report of the Intergovernmental Panel on
854 Climate Change) edited by: Solomon, S., Qin, D. Manning, M., Chen, Z., Marquis, M.,
855 Averyt, K. B., Tignor, M., and Miller, H. L., Cambridge Univ. Press, New York, USA,
856 131–217, 2007.
857
858 IPCC 2013 in Climate Change 2013: The Physical Science Basis. Working Group I
859 contribution to the IPCC fifth assessment report. Final Draft Underlying Scientific-
860 Technical Assessment, Cambridge University Press, Cambridge, United Kingdom and
861 New York, NY, USA, 2013.
862
863 Jorba, O., Pandolfi, M., Spada, M., Baldasano, J. M., Pey, J., Alastuey, A., Arnold, D.,
864 Sicard, M., Artinano, B., Revuelta, M. A., and Querol, X.: Meteorological overview and
865 transport patterns of the DAURE field campaign: link to PM observations, Atmos.
866 Environ., 77, 607-620, 2013.

JRC Report: Measurement of Elemental and Organic Carbon in Europe, Scientific and Technical Reports, EUR 23922 EN-2009, Joint Research Center, Ispra, Italy, 2009.

Laj, P., Klausen, J., Bilde, M., Plaß-Duelmer, C., Pappalardo, G., Clerbaux, C., Baltensperger, U., Hjorth, J., Simpson, D., Reimann, S., Coheur, P.-F., Richter, A., De Mazière, M., Rudich, Y., McFiggans, G., Torseth, K., Wiedensohler, A., Morin, S., Schulz, M., Allan, J.D., Attié, J.-L., Barnes, I., Birmili, W., Cammas, J. P., Dommen, J., Dorn, H.-P., Fowler, D., Fuzzi, S., Glasius, M., Granier, C., Hermann, M., Isaksen, I.S. A., Kinne, S., Koren, I., Madonna, F., Maione, M., Massling, A., Moehler, O., Mona, L., Monks, P.S., Müller, D., Müller, T., Orphal, J., Peuch, V.-H., Stratmann, F., Tanré, D., Tyndall, G., Abo Riziq, A., Van Roozendael, M., Villani, P., Wehner, B., Wex, H. and Zardini, A. A.: Measuring atmospheric composition change, Atmos. Environ., 43, 5351–5414, doi:10.1016/j.atmosenv.2009.08.020, 2009.

Marinoni, A., Cristofanelli, P., Calzolari, F., Roccato, F., Bonafe, U., Bonasoni, P.: Continuous measurements of aerosol physical parameters at the Mt. Cimone GAW station (2165 m a.s.l., Italy), Sci. Total. Environ., 391(2–3), 241–251, 2008.

Marcq, S., Laj, P., Roger, J.C., Villani, P., Sellegri, P., Bonasoni, P., Marinoni, A., Cristofanelli, P., Verza, G.P., Bergin, M.: Aerosol optical properties and radiative forcing in the high Himalaya based on measurements at the Nepal Climate Observatory—Pyramid site (5079 m a.s.l.), Atmos. Chem. Phys., 10 (13), 5859–5872, doi:10.5194/acp-10-5859-2010, 2010.

McKendry, I.G., Strawbridge, K., Karumudi, M.L., O'Neill, N., Macdonald, A.M., Leaitch, R., Jaffe, D., Cottle, P., Sharma, S., Sheridan, P., Ogren, J.: Californian forest fire plumes over Southwestern British Columbia: lidar, sunphotometry, and mountaintop chemistry observations, Atmos. Chem. Phys., 11, 465–477, doi:10.5194/acp-11-465-2011, 2011.

Millán, M.M., Artiñano, B., Alonso, L., Castro, M., Fernández-Patier, R., and Goberna, J.: Meso-meteorological Cycles of Air Pollution in the Iberian Peninsula, (MECAPIP), Contract EV4V-0097-E, Air Pollution Research Report 44, (Eur No. 14834) CEC-DG XII/E-1, Rue de la Loi, 200, 1040, Bruselas, 219 pp., 1992.

Millán, M.M., Salvador, R., Mantilla, E., and Kallos, G.: Photooxidant dynamics in the Mediterranean basin in summer: Results from European research projects, J. Geophys. Res., 102, 8811-8823, DOI: 10.1029/96JD03610, 1997.

Müller, T., Laborde, M., Kassel, G., and Wiedensolher, A.: Design and performance of a three-wavelenght LED-based total scatter and backscatter integrating nephelometer, Atmos. Meas. Tech., 4, 1291–1303, doi:10.5194/amt-4-1291-2011, 2011a.

Müller, T., Henzing, J.S., de Leeuw, G., Wiedensohler, A., Alastuey, A., Angelov, H., Bizjak, M., Collaud Coen, M., Engström, J.E., Gruening, C., Hillamo, R., Hoffer, A., Imre, K., Ivanow, P., Jennings, G., Sun, J.Y., Kalivitis, N., Karlsson, H., Komppula, M., Laj, P., Li, S.-M., Lunder, C., Marinoni, A., Martins dos Santos, S., Moerman, M., Nowak, A., Ogren, J. A., Petzold, A., Pichon, J. M., Rodriquez, S., Sharma, S., Sheridan, P.J., Teinil, K., Tuch, T., Viana, M., Virkkula, A., Weingartner, E., Wilhelm,

R., and Wang, Y. Q.: Characterization and intercomparison of aerosol absorption photometers: result of two intercomparison workshops, Atmos. Meas. Tech., 4, 245–268, doi:10.5194/amt-4-245-2011, 2011b.

Nyeki, S., Baltensperger, U., Colbeck, I., Jost, D.T., Weingartner, E., Gaggeler, H.W.: The Jungfraujoch high-alpine research station (3454 m) as a background clean continental site for the measurement of aerosol parameters, J. Geophys. Res., 103, 6097–6107, DOI: 10.1029/97JD03123, 1998.

Ogren, J.A., Andrews, E., McComiskey, A., Sheridan, P., Jefferson, A., Fiebig, M.: New insights into aerosol asymmetry parameter, In: Proceedings of the 16th ARM Science Team Meeting, Albuquerque, NM, USA, 2006.

Pandolfi, M., Cusack, M., Alastuey, A. and Querol, X.: Variability of aerosol optical properties in the Western Mediterranean Basin, Atmos. Chem. Phys., 11, 8189–8203, doi:10.5194/acp-11-8189-2011, 2011.

Pandolfi, M., Querol, X., Alastuey, A., Jimenez, J. L., Jorba, O., Day, D., Ortega, A., Cubison, M. J., Comerón, A., Sicard, M., Mohr, C., Prévôt, A. S. H., Minguillón, M. C., Pey, J., Baldasano, J. M., Burkhart, J. F., Seco, R., Peñuelas, J., van Drooge, B. L., Artiñano, B., Di Marco, C., Nemitz, E., Schallhart, S., Metzger, A., Hansel, A., Lorente, J., Ng, S., Jayne, J., and Szidat, S.: Effects of sources and meteorology on particulate matter in the Western Mediterranean Basin: An overview of the DAURE campaign, J. Geophys. Res. Atmos., 119, doi:10.1002/2013JD021079, 2014.

942 Pereira, S. N.,Wagner, F., and Silva, A. M.: Seven year of measurements of aerosol
943 scattering properties, near the surface, in the southwestern Iberia Peninsula, Atmos.
944 Chem. Phys., 11, 17—29, doi:10.5194/acp-11-17-2011, 2011.
945
946 Pérez, C., Sicard, M., Jorba, O., Comerón, A., and Baldasano J.M.: Summertime re-
947 circulations of air pollutants over the northeastern Iberian coast observed from
948 systematic EARLINET lidar measurements in Barcelona, Atmos. Environ., 38, 3983–
949 4000, doi:10.1016/j.atmosenv.2004.04.010, 2004.
950
951 Pérez, N., Pey, J., Castillo, S., Viana, M., Alastuey, A., and Querol, X.: Interpretation of
952 the variability of levels of regional background aerosols in the Western Mediterranean,
953 Sci. Total Environ., 407, 527–540, doi: 10.1016/j.scitotenv.2008.09.006, 2008.
954
955 Petzold, A. and Schönlinner, M.: Multi-angle absorption photometry – a new method
956 for the measurement of aerosol light absorption and atmospheric black carbon, J.
957 Aerosol Sci., 35, 421–441, DOI:10.1016/j.jaerosci.2003.09.005, 2004.
958
959 Pey, J., Pérez, N., Castillo, S., Viana, M., Moreno, T., Pandolfi, M., López-Sebastián, J.
960 M., Alastuey, A., and Querol, X.: Geochemistry of regional background aerosols in the
961 Western Mediterranean, Atmos. Res., 94, 422–435,
962 DOI:10.1016/j.atmosres.2009.07.001, 2009.
963
964 Pey, J., Querol, X., Alastuey, A., Forastiere, F., and Stafoggia, M.: African dust
965 outbreaks over the Mediterranean Basin during 2001–2011: PM10 concentrations,

966 phenomenology and trends, and its relation with synoptic and mesoscale meteorology,
967 Atmos. Chem. Phys., 13, 1395-1410, doi:10.5194/acp-13-1395-2013, 2013
968
969 Polissar, A.V., Hopke, P.K., Malm, W.C., Sisler, J.F.: Atmospheric aerosols over
970 Alaska: 2. Elemental Composition and Sources, J. Geophys. Res., 103, 19045-19057,
971 DOI: 10.1029/98JD01212, 1998.
972
973 Querol, X., Alastuey, A., Lopez-soler, A., Plana, F. and Puicercus, J. A.: Daily
974 evolution of sulphate aerosols in a rural area, northeastern Spain - elucidation of an
975 atmospheric reservoir effect, Environ. Pollut., 105, 397–967 407, doi:10.1016/S0269-
976 7491(99)00037-8, 1999.
977
978
979 Querol, X., Pey, J., Minguillón, M. C., Pérez, N., Alastuey, A., Viana, M., Moreno, T.,
980 Bernabé, R.M., Blanco, S., Cárdenas, B., Vega, E., Sosa, G., Escalona, S., Ruiz, H., and
981 Artñano, B.: PM speciation and sources in Mexico during the MILAGRO-2006
982 Campaign, Atmos. Chem. Phys., 8, 111–128, doi:10.5194/acp-8-111-2008, 2008.
983
984 Querol, X., Alastuey, A., Pey, J., Cusack, M., Pérez, N., Mihalopoulos, N., Theodosi,
985 C., Gerasopoulos, E., Kubilay, N., and Koçak, M.: Variability in regional background
986 aerosols within the Mediterranean, Atmos. Chem. Phys., 9, 4575-4591,
987 doi:10.5194/acp-9-4575-2009, 2009.
988
989 Querol, X., Alastuey, A., Viana, M., Moreno, T., Reche, C., Minguillón, M. C., Ripoll,
990 A., Pandolfi, M., Amato, F., Karanasiou, A., Pérez, N., Pey, J., Cusack, M., Vázquez,

991 R., Plana, F., Dall'Osto, M., de la Rosa, J., Sánchez de la Campa, A., Fernández-
992 Camacho, R., Rodríguez, S., Pio, C., Alados-Arboledas, L., Titos, G., Artíñano, B.,
993 Salvador, P., García Dos Santos, S., and Fernández Patier, R.: Variability of
994 carbonaceous aerosols in remote, rural, urban and industrial environments in Spain:
995 implications for air quality policy, Atmos. Chem. Phys., 13, 6185-6206,
996 doi:10.5194/acp-13-6185-2013, 2013.
997
998 Quinn, P.K., and Bates, T.S.: Regional aerosol properties: Comparisons of boundary
999 layer measurements from ACE 1, ACE 2, Aerosols99, INDOEX, ACE Asia, TARFOX,
1000 and NEAQS, J. Geophys. Res., 110(D14), D14202, DOI: 10.1029/2004JD004755,
1001 2005.
1002
1003 Reche, C., Querol, X., Alastuey, A., Viana, M., Pey, J., Moreno, T., Rodríguez, S.,
1004 González, Y., Fernández-Camacho, R., de la Rosa, J., Dall'Osto, M., Prévôt, A. S. H.,
1005 Hueglin, C., Harrison, R. M., and Quincey, P.: New considerations for PM, Black
1006 Carbon and particle number concentration for air quality monitoring across different
1007 European cities, Atmos. Chem. Phys., 11, 6207–6227, doi:10.5194/acp-11-6207-2011,
1008 2011.
1009
1010 Ripoll, A., Pey, J., Minguillón, M. C., Pérez, N., Pandolfi, M., Querol, X., and Alastuey,
1011 A.: Three years of aerosol mass, black carbon and particle number concentrations at
1012 Montsec (southern Pyrenees, 1570 m a.s.l.), Atmos. Chem. Phys., 14, 4279-4295,
1013 doi:10.5194/acp-14-4279-2014, 2014.
1014

1015 Rodríguez, S., Querol, X., Alastuey, A., Kallos, G., and Kakaliagou, O.: Saharan dust
1016 contributions to PM10 and TSP levels in Southern and Eastern Spain, Atmos. Environ.,
1017 35, 2433–2447, 2001.
1018
1019 Rodríguez, S., Querol, X., Alastuey, A., Viana, M.M., Alarcón, M., Mantilla, E., Ruiz,
1020 CR.: Comparative PM10-PM2.5 source contribution study at rural, urban and industrial
1021 sites during PM episodes in Eastern Spain, Sci. Tot. Environ., 26, 328(1-3), 95-113,
1022 DOI:10.1016/S0048-9697(03)00411-X, 2004.
1023
1024 Rodríguez, S., Alastuey, A., Alonso-Pérez, S., Querol, X., Cuevas, E., Abreu-Afonso,
1025 J., Viana, M., Pérez, N., Pandolfi, M., and de la Rosa, J.: Transport of desert dust mixed
1026 with North African industrial pollutants in the subtropical Saharan Air Layer, Atmos.
1027 Chem. Phys., 11, 6663-6685, doi:10.5194/acp-11-6663-2011, 2011.
1028
1029 Schuster, G. L., Dubovik, O., and Holben, B. N.: Ångström exponent and bimodal
1030 aerosol size distributions, J. Geophys. Res., 111, D07207, doi:101029/2005JD006328,
1031 2006.
1032
1033 Seco, R., Peñuelas, J., Filella, I., Llusià, J., Molowny-Horas, R., Schallhart, S., Metzger,
1034 A., Müller, M. and Hansel, A.: Contrasting winter and summer VOC mixing ratios at a
1035 forest site in the Western Mediterranean Basin: the effect of local biogenic emissions,
1036 Atmos. Chem. Phys., 11, 13161–13179, doi:10.5194/acp-11-13161-2011, 2011.
1037
1038

1039 Sellegri, K., P. Laj, R. Dupuy, M. Legrand, S. Preunkert, and J.-P. Putaud: Size-
1040 dependent scavenging efficiencies of multicomponent atmospheric aerosols in clouds, J.
1041 Geophys. Res., 108, 4334, doi:10.1029/2002JD002749, D11, 2003.
1042
1043 Singh, R. P., Dey, S., Tripathi, S. N., Tare, V., and Holben, B. N.: Variability of aerosol
1044 parameters over Kanpur city, northern India, J. Geophys. Res., 109, D23206,
1045 doi:10.1029/2004JD004966, 2004.
1046
1047 Targino, A.C., Noone, K.J., Ostrom, E.: Airborne in-situ characterization of dry aerosol
1048 optical properties in a multisource influenced marine region, Tellus, 57B, 247–260,
1049 DOI: 10.1111/j.1600-0889.2005.00147.x, 2005.
1050
1051 Vaisala Oyj.: Humidity Conversion Formulas, published by Vaisala, Helsinki,
1052 http://www.vaisala.com/Vaisala%20Documents/Application%20notes/Humidity_Conve
1053 rsion_Formulas_B210973EN-F.pdf, 2013.
1054
1055 Venzac, H., Sellegri, K., Villani, P., Picard, D., and Laj P.: Seasonal variation of aerosol
1056 size distributions in the free troposphere and residual layer at the puy de Dome station,
1057 France, Atmos. Chem. Phys., 9, 1465–1478, doi:10.5194/acp-9-1465-2009, 2009.
1058
1059
1060
1061
1062
1063
1064
1065

**Table 1**: Acronyms used in this work

| **Acronyms** |
|---|
| |
| *Extensive aerosol optical properties* |
| $\sigma_{sp}$: particle scattering |
| $\sigma_{bsp}$: particle backscattering |
| $\sigma_{ap}$: particle absorption |
| |
| *Intensive aerosol optical properties* |
| SSA: single scattering albedo |
| SAE: scattering Ångström exponent |
| B/S: backscatter-to-scatter ratio |
| g: asymmetry parameter |
| MAC: mass absorption cross section |
| MSCS: mass scattering cross section |
| |
| *Concentration measurements* |
| BC: black carbon |
| EC: elemental carbon |
| $PM_1$: particles with aerodynamic diameter < 1 μm |
| $PM_{10}$: particles with aerodynamic diameter < 10 μm |
| *Measurement sites* |
| MSC: Montsec (NE Spain; mountaintop measurement site) |
| MSY: Montseny (NE Spain; Regional background measurement site) |
| *Air masses* |
| AA: Atlantic Ocean Advections |
| NAF: North Africa |
| WREG: winter-regional scenario |
| SREG: summer-regional scenario |
| *Others* |
| WMB: Western Mediterranean Basin |
| PBL: Planetary Boundary Layer |
| FT: Free troposphere |

**Table 2**: Statistics of the considered aerosol components and parameters for the period June 2011 – June 2013 at Montsec site (*all data*). The wavelength (λ) is given in [nm]; Scattering ($\sigma_{sp}$), backscattering ($\sigma_{bsp}$) and absorption coefficients ($\sigma_{ap}$) are given in [$Mm^{-1}$]; Backscattering-to-scattering ratio (B/S), asymmetry parameter (*g*), single scattering albedo (SSA) and Ångström exponent (SAE) are dimensionless; $PM_1$ concentrations are given in [$\mu gm^{-3}$]; MAC is expressed in [$m^2/g$]. Statistics based on hourly mean values (24h for MAC). Optical data were referenced to STP ($T_{standard}$=273.15 K and $P_{standard}$=1013.25 hPa).

| Hourly base | λ | counts | mean | SD | Median ($50^{th}$ perc.) | min | max | skewness | percentiles | | | | |
|---|---|---|---|---|---|---|---|---|---|---|---|---|---|
| | | | | | | | | | 1 | 10 | 25 | 75 | 99 |
| $\sigma_{sp}$ | 635 | 10014 | 18.9 | 20.8 | 11.2 | 0.1 | 161.1 | 1.83 | 0.2 | 1.1 | 3.5 | 28.3 | 89.8 |
| | 525 | 10014 | 25.4 | 27.5 | 15.1 | 0.1 | 222.2 | 1.68 | 0.1 | 1.6 | 4.5 | 38.6 | 118.5 |
| | 450 | 10014 | 32.3 | 34.7 | 19.3 | 0.1 | 276.2 | 1.62 | 0.1 | 2.0 | 5.6 | 49.6 | 143.6 |
| $\sigma_{bsp}$ | 635 | 10014 | 2.6 | 2.8 | 1.7 | 0.0 | 17.1 | 1.25 | 0.1 | 0.2 | 0.4 | 4.3 | 11.1 |
| | 525 | 10014 | 3.1 | 3.2 | 1.9 | 0.0 | 36.4 | 1.31 | 0.1 | 0.2 | 0.5 | 5.1 | 12.8 |
| | 450 | 10014 | 3.6 | 3.9 | 2.2 | 0.0 | 96.0 | 1.21 | 0.1 | 0.2 | 0.5 | 6.0 | 14.6 |
| B/S | 635 | 8612 | 0.16 | 0.09 | 0.15 | 0.02 | 0.99 | 4.03 | 0.04 | 0.10 | 0.12 | 0.18 | 0.58 |
| | 525 | 8864 | 0.13 | 0.07 | 0.13 | 0.01 | 0.98 | 4.78 | 0.04 | 0.09 | 0.11 | 0.15 | 0.44 |
| | 450 | 8761 | 0.12 | 0.06 | 0.11 | 0.01 | 1.00 | 4.95 | 0.03 | 0.07 | 0.10 | 0.13 | 0.36 |
| $\sigma_{ap}$ | 637 | 13712 | 1.5 | 1.4 | 1.0 | 0.0 | 12.6 | 1.45 | 0.0 | 0.1 | 0.3 | 2.4 | 6.2 |
| *g* | 635 | 8587 | 0.53 | 0.16 | 0.54 | -0.99 | 0.93 | -2.51 | -0.10 | 0.39 | 0.49 | 0.60 | 0.85 |
| | 525 | 8858 | 0.59 | 0.13 | 0.59 | -0.92 | 0.94 | -3.25 | 0.09 | 0.49 | 0.55 | 0.64 | 0.85 |
| | 450 | 8755 | 0.62 | 0.11 | 0.62 | -0.79 | 0.95 | -2.15 | 0.20 | 0.53 | 0.58 | 0.66 | 0.88 |
| SAE | 450-635 | 9561 | 1.56 | 0.88 | 1.65 | -1.96 | 5.99 | 0.30 | -1.14 | 0.56 | 1.22 | 1.90 | 4.69 |
| SSA | 635 | 6123 | 0.92 | 0.03 | 0.93 | 0.45 | 0.99 | -2.59 | 0.81 | 0.89 | 0.91 | 0.94 | 0.97 |
| MAC | 637 | 384 | 10.9 | 3.5 | 11.1 | 2.4 | 20.8 | 0.21 | 3.6 | 6.2 | 8.2 | 13.2 | 19.8 |
| MSCS | 635 | 228 | 2.5 | 1.4 | 2.4 | 0.1 | 7.5 | 0.66 | 0.2 | 0.7 | 1.3 | 3.4 | 6.8 |
| | 525 | 228 | 3.3 | 1.9 | 3.2 | 0.1 | 10.3 | 0.74 | 0.2 | 1.1 | 1.8 | 4.6 | 9.3 |
| | 450 | 228 | 4.2 | 2.4 | 4.0 | 0.2 | 12.9 | 0.73 | 0.3 | 1.5 | 2.2 | 5.9 | 11.8 |
| $PM_1$ | - | 10949 | 5.3 | 4.5 | 4.0 | 0.1 | 49.9 | 2.06 | 0.5 | 1.4 | 1.9 | 7.2 | 21.8 |

**Figure captions:**

**Figure 1**: Location of the Montsec (MSC; remote-mountaintop site) and Montseny (MSY; regional background) measurement sites. Barcelona is also shown. Yellow dots are meteorological stations (Observatory (800 m a.s.l.), Os de Balaguer (576 m) and Vallfogona de Balaguer (238 m)). Air mass backtrajectories from Atlantic Ocean (AA), regional (REG) and North Africa (NAF).

**Figure 2**: Diurnal cycles and cluster analysis of scattering ($\sigma_{sp}$ at 635 nm), absorption ($\sigma_{ap}$ at 637 nm), single scattering albedo (SSA at 635 nm), scattering Ångström exponent (SAE calculated between 450 and 635 nm) and $PM_1$ concentrations measured at Montsec site (MSC; black lines) and at Montseny regional background site (MSY; grey lines). Atmospheric scenarios are: Atlantic advection (AA), African dust outbreaks (NAF), winter regional anticyclonic episodes (WREG) and summer regional recirculation episodes (SREG).

**Figure 3**: Seasonal diurnal cycles of relative humidity, potential temperature and water vapour mixing ratio measured at Montsec (1570 m a.s.l.), Montsec Observatory (800 m), Os de Balaguer (576 m) and Vallfogona de Balaguer (238 m). Also shown are the diurnal cycles of the planetary boundary layer height (PBL) from HYSPLIT and of the potential temperature and actual temperature gradients. Yellow rectangles highlight the time of the day approach for the identification of FT air proposed in Andrews et al. (2011) and used in this work (from 3:00 to 9:00 local time). Times are reported in GMT. Grey rectangles highlight hours when the MSC station was within the planetary boundary layer. Meteorological data at the 4 stations were available from 1$^{th}$ Jan 2011 to 31 Dec 2012.

**Figure 4**: Diurnal cycles of normalized aerosol scattering at 550 nm measured at MSC as a function of the seasons: winter (DJF), fall (SON), spring (MAM) and summer (JJA).

**Figure 5**: Aerosol optical properties for *all-data* and *FT-data* data. Data are reported at 550 nm. Red=*all-data*, Yellow=*FT-data*. Horizontal lines within the boxes are the medians (50th percentile), edges of box are 25th and 75th percentiles, and whiskers are 5th and 95th percentiles. Ångström exponent is calculated for 450/635 nm pair. For

MSC values are calculated for the whole period considered here (ALL), and for fall (SON), winter (DJF), spring (MAM) and summer (JJA). The percentage values represent the relative difference between the medians calculated for *all-data* and *FT-data*. Green bold numbers indicate statistically significant differences (p-value<0.05); blue bold numbers highlight marginally significant differences (p<0.1); black numbers indicate differences which were not statistically significant (p>0.1). The red and yellow rectangles within the blue areas on the right of each figure represent the range of variability of the medians presented by Andrews et al. (2011) calculated for sites in the western hemisphere (W), Europe (EU) and eastern hemisphere (E).

**Figure 6**: Correlation between the frequency distribution of aerosol scattering coefficients ($\sigma_{sp}$) at 635 nm and backscattering coefficient ($\sigma_{bsp}$ at 635 nm), absorption coefficient ($\sigma_{ap}$ at 637 nm), $PM_1$ concentrations ($PM_1$), asymmetry parameter (*g* at 635 nm), scattering Ångström exponent (SAE; 450-635 nm), single scattering albedo (SSA at 635 nm). Correlations are presented for all data (ALL) and for the different atmospheric scenarios (Atlantic Advection, AA; Saharan dust outbreaks, NAF; summer regional recirculation scenario, SREG; and winter anticyclonic scenario, WREG). Frequency count (%) and the absolute number of hourly values (counts) in each been are reported.

**Figure 7**: Scattering coefficient ($\sigma_{sp}$) distribution at 635 nm as a function of scattering Ångström exponent (SAE) by atmospheric scenarios (a) and by levels of $PM_1/PM_{10}$ ratio (b). Dark data points indicate SAE>4.

**Figure 8**: Monthly mean mass absorption cross section (MAC) and mass scattering cross section (MSCS) at MSC station and occurrence (%) of the main atmospheric scenarios (AA: Atlantic advections; NAF: Saharan dust outbreaks; SREG: summer regional recirculation scenarios; WREG: winter anticyclonic scenarios). Bars represent 95 % confidence intervals.

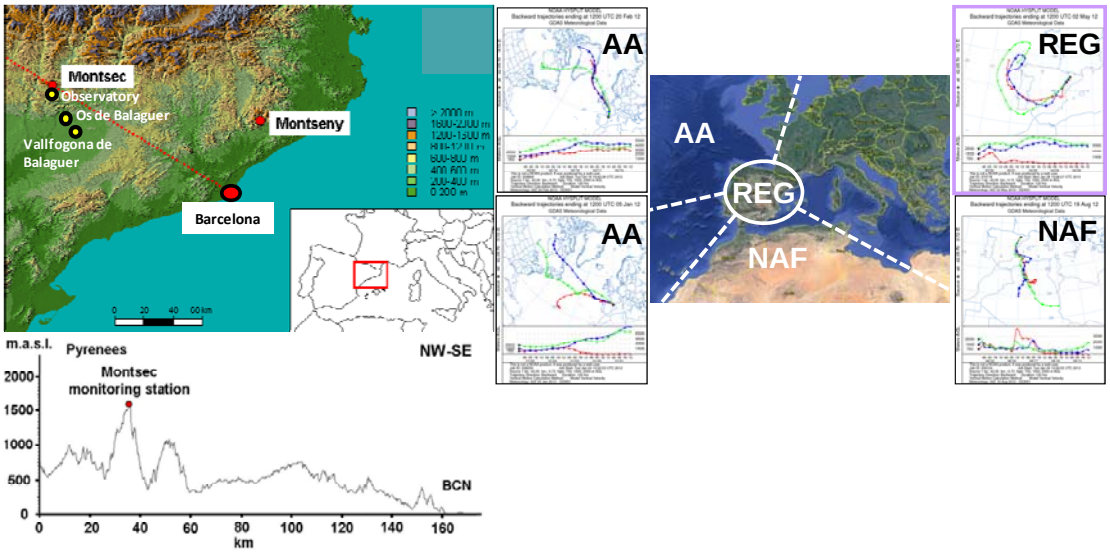
Montsec
Observatory
Os de Balaguer
Vallfogona de Balaguer
Montseny
Barcelona
AA
AA
REG
NAF
REG
NAF
NW-SE
m.a.s.l.
Pyrenees
Montsec
monitoring station
BCN
2000
1500
1000
500
0
0
20
40
60
80
100
120
140
160
km

**Figure 1**

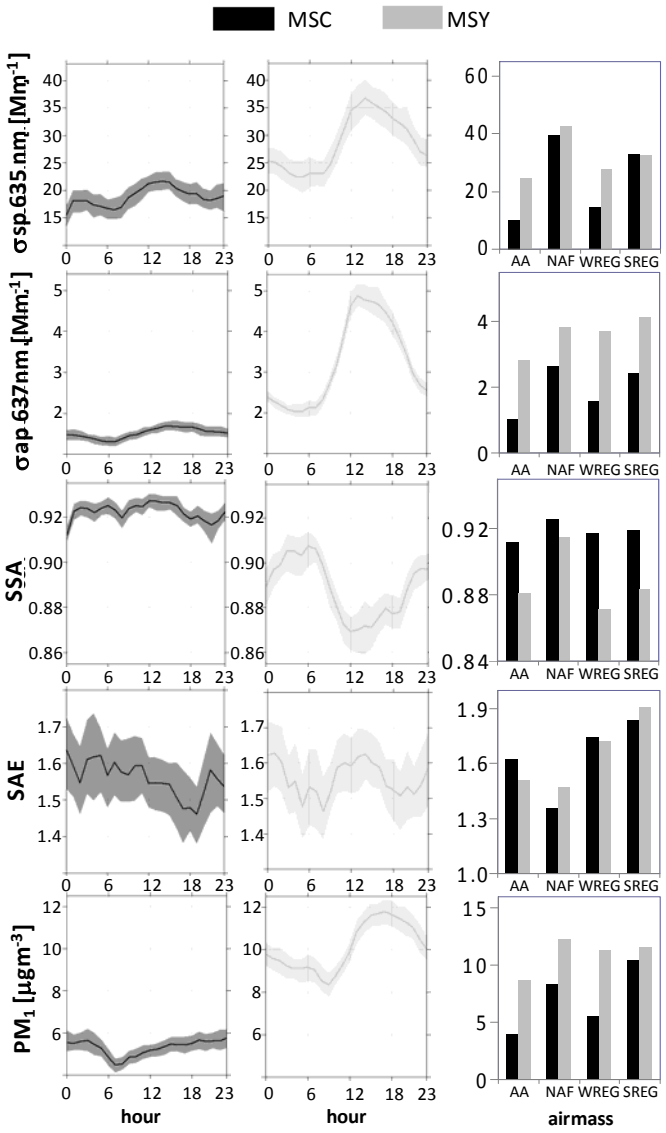
MSC
MSY
σsp.635.nm.[Mm-1]
σap.637nm.[Mm-1]
SSA
SAE
PM1 [µgm-3]
AA NAF WREG SREG
hour
hour
airmass

**Figure 2**

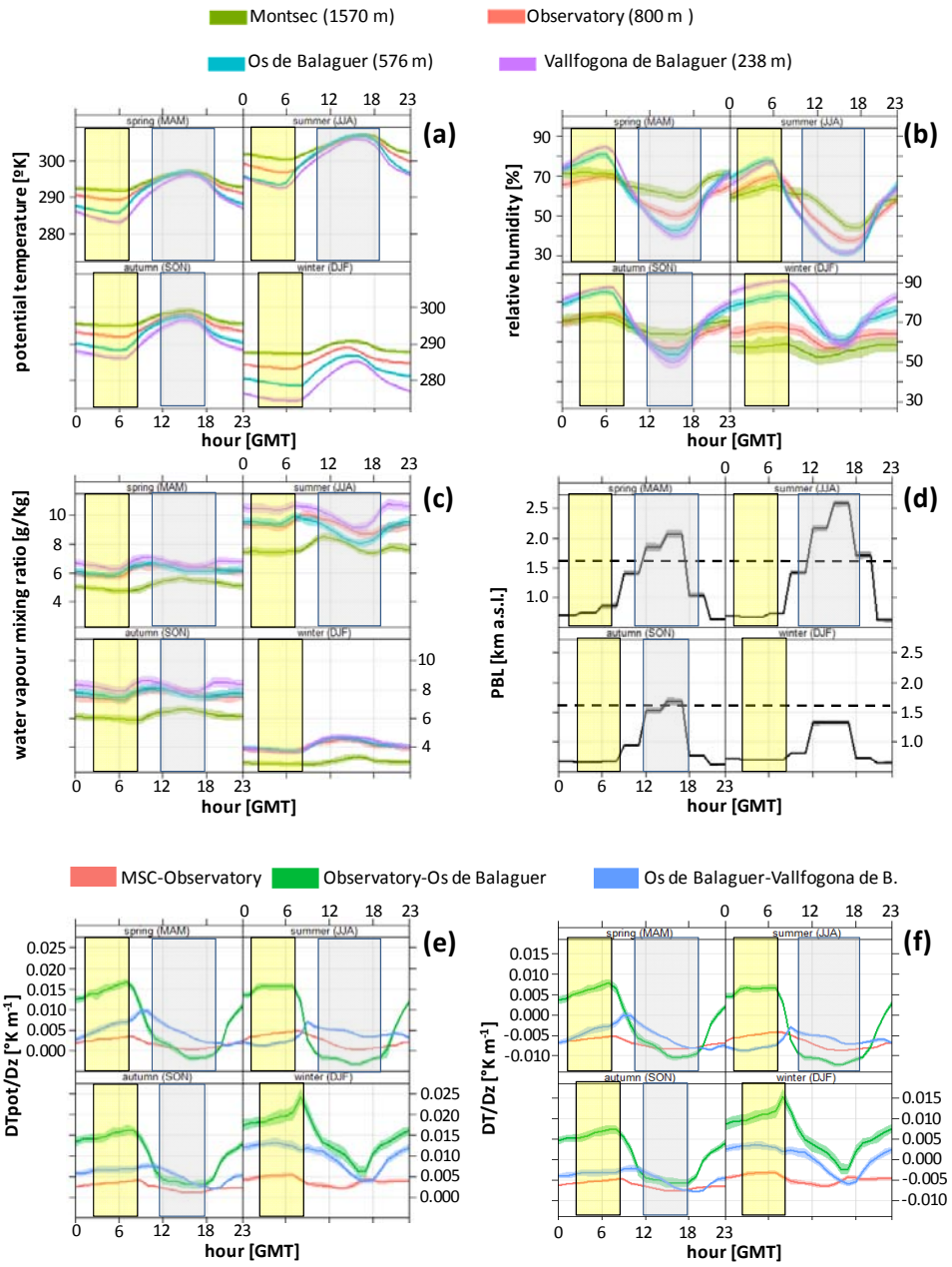
Montsec (1570 m)
Observatory (800 m )
Os de Balaguer (576 m)
Vallfogona de Balaguer (238 m)
(a)
(b)
(c)
(d)
(e)
(f)
potential temperature [ºK]
relative humidity [%]
water vapour mixing ratio [g/Kg]
PBL [km a.s.l.]
DTpot/Dz [°K m-1]
DT/Dz [°K m-1]
spring (MAM)
summer (JJA)
autumn (SON)
winter (DJF)
hour [GMT]
MSC-Observatory
Observatory-Os de Balaguer
Os de Balaguer-Vallfogona de B.

**Figure 3**

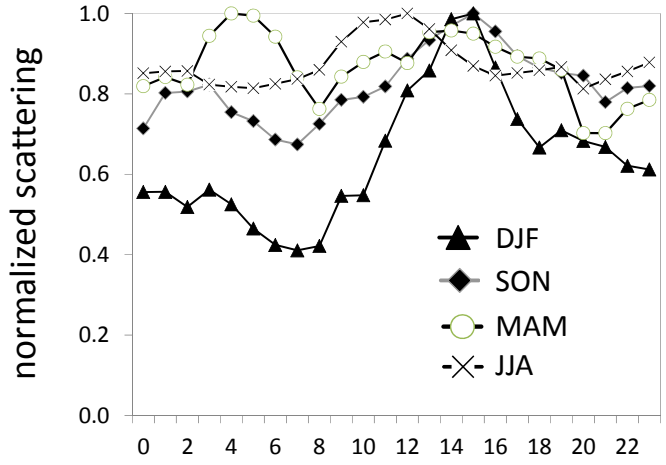
normalized scattering
1.0
0.8
0.6
0.4
0.2
0.0
0
2
4
6
8
10
12
14
16
18
20
22
DJF
SON
MAM
JJA

**Figure 4**

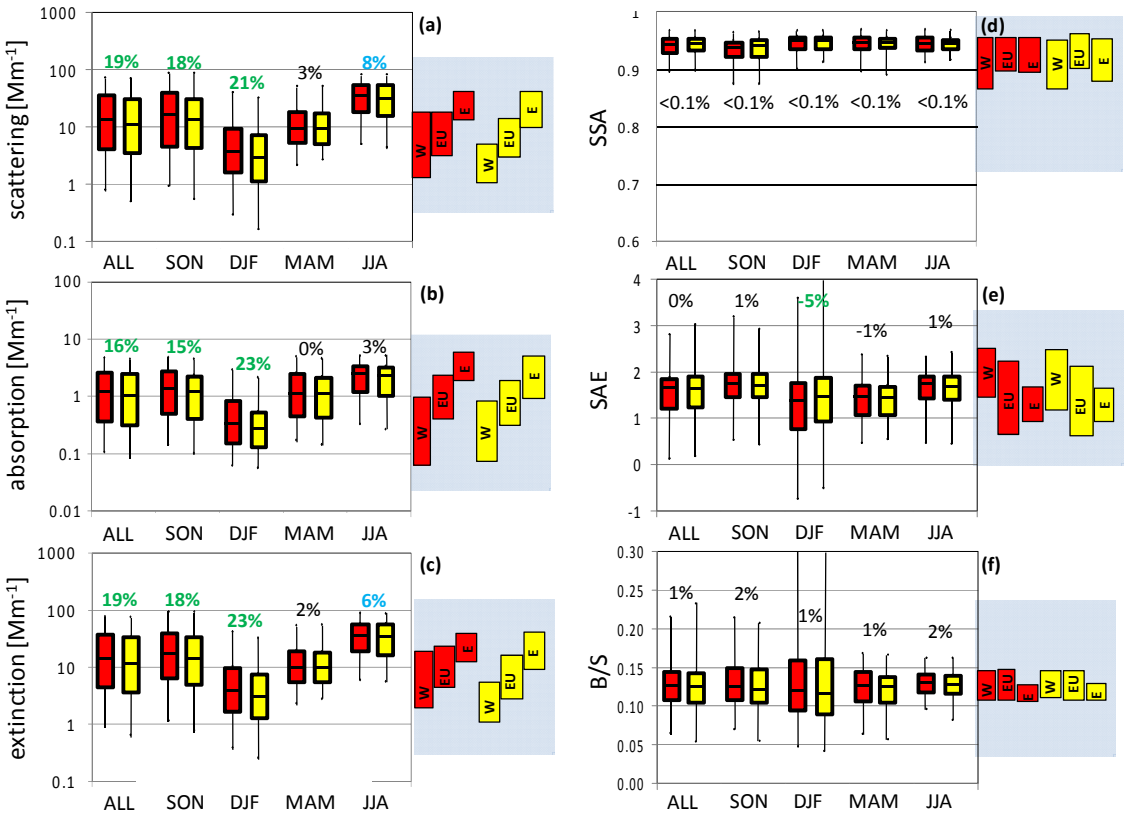
scattering [Mm-1]
absorption [Mm-1]
extinction [Mm-1]
SSA
SAE
B/S
(a)
(b)
(c)
(d)
(e)
(f)
ALL
SON
DJF
MAM
JJA
W
EU
E
19%
18%
21%
3%
8%
16%
15%
23%
0%
3%
19%
18%
23%
2%
6%
<0.1%
0%
1%
-5%
-1%
1%
1%
2%
1%
1%
2%

**Figure 5**

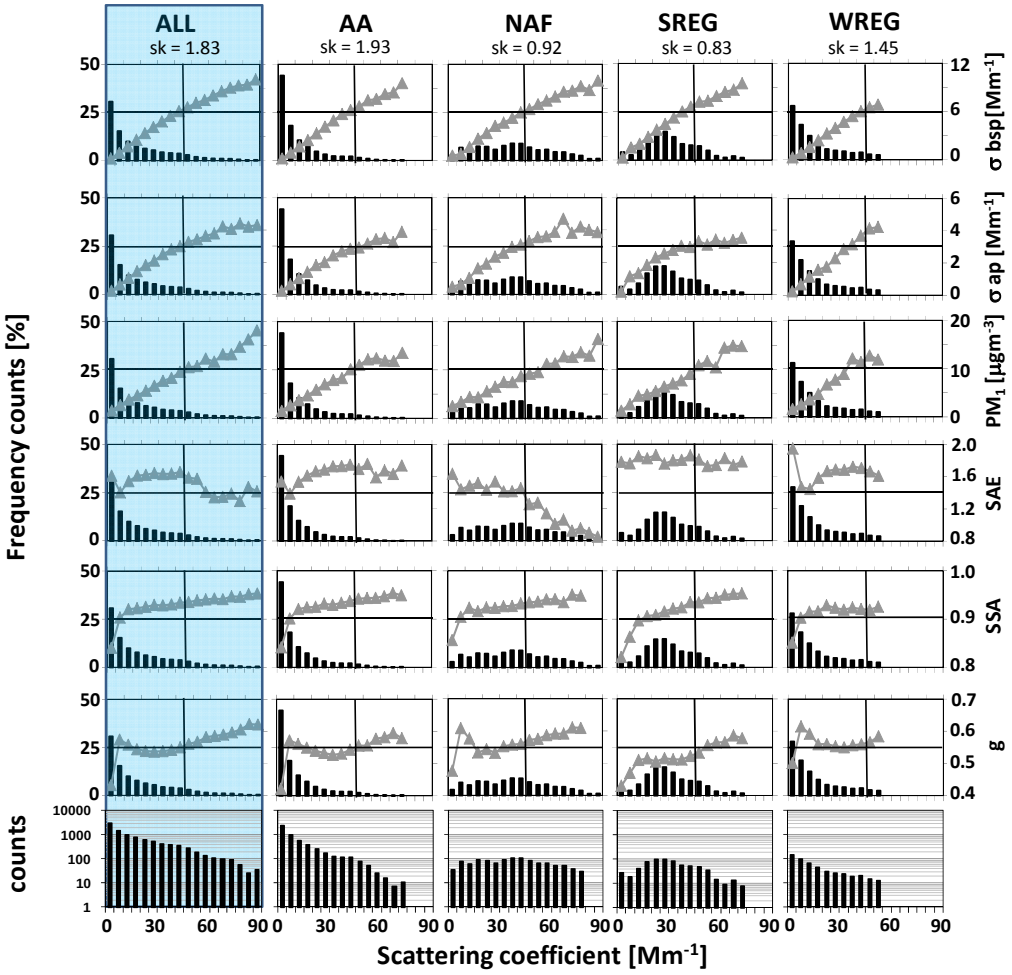
ALL
sk = 1.83
AA
sk = 1.93
NAF
sk = 0.92
SREG
sk = 0.83
WREG
sk = 1.45
Frequency counts [%]
σ bsp[Mm-1]
σ ap [Mm-1]
PM1 [µgm-3]
SAE
SSA
g
counts
Scattering coefficient [Mm-1]

**Figure 6**

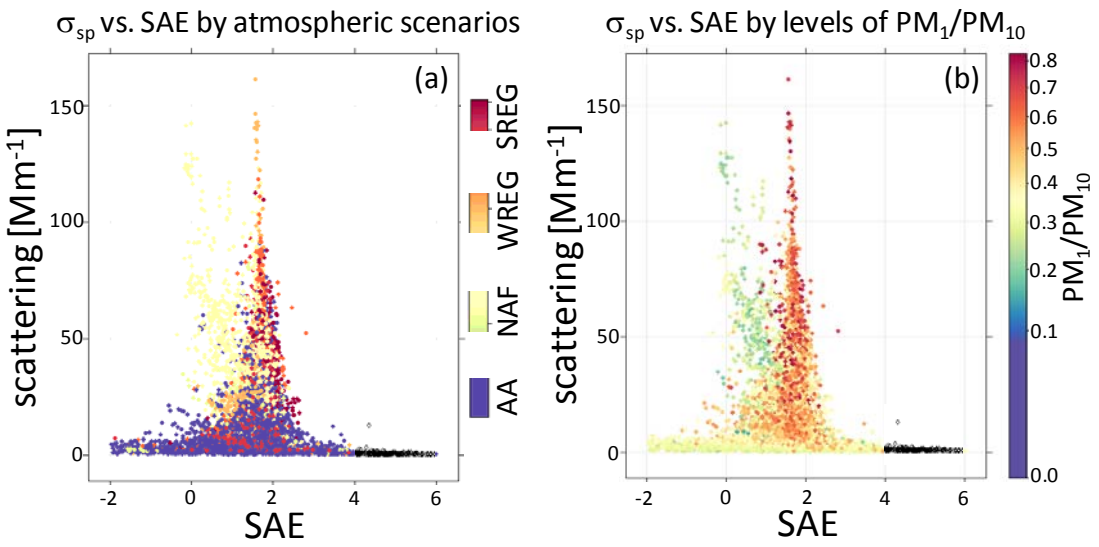
σsp vs. SAE by atmospheric scenarios
(a)
scattering [Mm-1]
SAE
SREG
WREG
NAF
AA
σsp vs. SAE by levels of PM1/PM10
(b)
PM1/PM10
0.8
0.7
0.6
0.5
0.4
0.3
0.2
0.1
0.0

**Figure 7**

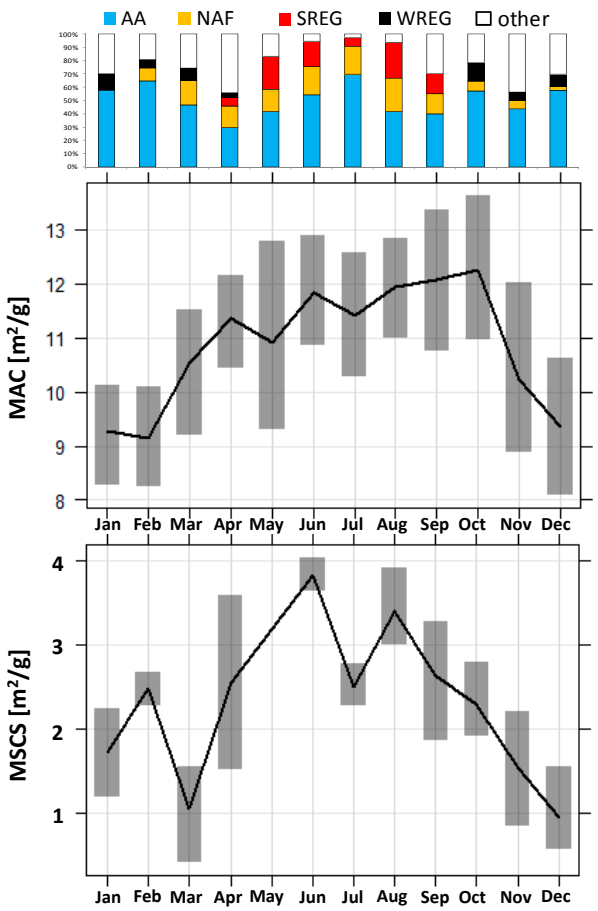
AA
NAF
SREG
WREG
other
MAC [m²/g]
MSCS [m²/g]
Jan
Feb
Mar
Apr
May
Jun
Jul
Aug
Sep
Oct
Nov
Dec

**Figure 8**